Journal of Statistical Physics, Vol. 119, Nos. 5/6, June 2005 (© 2005)
DOI: 10.1007/s10955-005-4405-2

Bifurcations in a System of Interacting Fronts

A. Amann[1,2] **and E. Schöll**[1]

Received June 10, 2004; accepted February 25, 2005

We show that the bifurcation scenario in a high-dimensional system with interacting moving fronts can be related to the universal *U-sequence* which is known from the symbolic analysis of iterated one-dimensional maps. This connection is corroborated for a model of a semiconductor superlattice, which describes the complex dynamics of electron accumulation and depletion fronts. By a suitable Poincaré section we reduce the dynamics to a low-dimensional iterated map, for which in the most elementary case the bifurcation points can be determined analytically.

KEY WORDS: Front dynamics; U-sequence; semiconductor superlattice.

1. INTRODUCTION

Moving fronts are the source of complex self-organized patterns in a broad range of nonlinear systems.[1] Starting from classical water waves, fronts appear in many different forms in physics, such as the phase transition fronts in crystal growth[2] or as interstellar conduction fronts[3] in astronomy. Prominent examples for front dynamics in chemical systems are the famous Belousov–Zhabotinskii reaction[4,5] or combustion waves.[6] Furthermore fronts are often a key element in the self-organization processes in biological systems, for example the excitation wave in cardiac tissue[7] or during morphogenesis.[8] It is therefore an important task of nonlinear science to identify the basic features which are responsible for the similarities and differences observed in a variety of front systems and to provide a unified theory of front dynamics, which may explain the observed patterns irrespective of the particular system at hand.

[1]Institut für Theoretische Physik, Technische Universität Berlin, Hardenbergstraße 36, 10623 Berlin, Germany; e-mail: schoell@physik.tu-berlin.de
[2]Present address: Tyndall National Institute, Lee Maltings, Cork, Ireland; e-mail: amann@physik.tu-berlin.de

Since the 1960s many aspects of single isolated fronts have been studied in the physical and mathematical literature. Thus a detailed understanding of the generation, the shape, and the propagation of single fronts in an infinite medium was obtained in the context of simplified mathematical models in one or two-dimensions.[9,10] In particular, the importance of the non-equilibrium aspects was realized, and important notions like the distinction between bistable, excitable and oscillatory media were introduced.

In real world systems, however, multiple fronts often coexist, and the interaction between fronts may lead to sophisticated self-organized patterns, such as the ones shown in Fig. 1. To understand the relevant mechanisms, it would be desirable to again obtain a simple mathematical picture, which is capable of identifying the key elements that lead to a particular pattern, but so far no unifying theory exists. Considerable effort in this direction has been made concerning the problem of turbulence in fluid systems, which is often quoted to be the "last great unsolved problem of classical physics".[11] In spite of major advances, a unified theory for turbulence is still not available and it is also not clear, how the results in this area could be carried over to more general front systems.

Semiconductor devices have a long tradition as practically relevant nonlinear model systems.[12–19] Fueled by their enormous technological relevance and economic success, semiconductor materials have become one of the best studied objects in solid state physics. The manufacturing technology for building small well-defined semiconductor structures of high purity has steadily improved during the last decades, and structures in the sub-micron range are commercially available today.

In a semiclassical description, the dynamically relevant quantities in semiconductor devices are typically the densities of the free electrons or holes, the electric field or the local temperature. Often the microscopic charge transport equations in such devices are nonlinear[14,19] and may give rise to a local regime of negative differential conductivity (NDC) in the local current density vs electric field characteristic. An N-shaped current density vs electric field characteristic typically leads to charge accumulation and depletion fronts forming electric field domains in the direction parallel to the current. Moving charge fronts connected with traveling high-field domains appear for instance in the Gunn diode,[12] or in low-temperature impurity breakdown in p-Ge, for which simple front models have been derived.[21,20]

As a specific illustration, in the following we will consider semiconductor superlattices, which consist of alternating layers of two types of materials with different band gaps, resulting in modulated energies in the form of barriers and quantum wells. Typically AlAs is used as the bar-

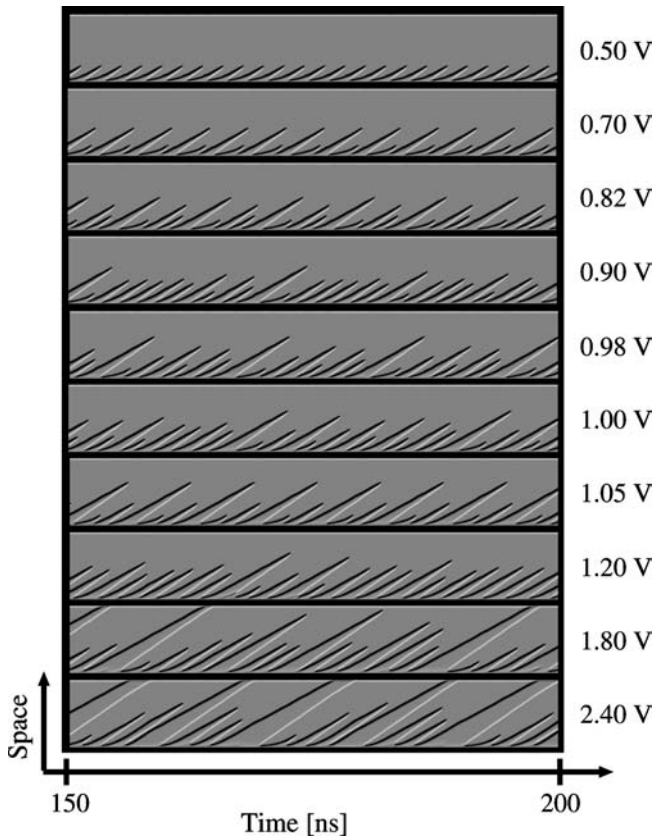

Fig. 1. Space–time plots of the dynamic evolution of the charge density for various voltages (0.50 V–2.4 V) in a semiconductor superlattice as described in Section 2. Regions of electron accumulation and depletion are denoted by white and black, respectively. In each panel the emitter (collector) is located at the lower (upper) edge. Simulations with parameters given in the text, and contact conductivity $\sigma = 0.5\,\Omega^{-1}\mathrm{m}^{-1}$.

rier material and GaAs or $Al_xGa_{1-x}As$ is used as the well material. The microscopic equations and the basic front dynamics in such systems are discussed in refs. 22 and 23. From the technological aspect, superlattices may serve as a source for Gigahertz electronic oscillations.[24–26] Recently, the successful operation of a so called "quantum cascade laser",[27,28] which is a specifically modified superlattice, has sparked further interest in this type of structures. Superlattices have also been shown to be prominent examples of non-KAM behavior in quantum chaos.[29]

It is the purpose of the present work to gain a better understanding of interacting fronts, by using the semiconductor superlattice as a

particularly simple, but nevertheless technologically relevant model system. Our main focus is on general results which also apply to a variety of other front system in physics, chemistry, and biology. The main achievement of the present work is to establish the connection between the dynamics in an interacting front system and the bifurcations of a low-dimensional iterated map. It will be shown that in the case of a superlattice, a simple mathematical description in the framework of a tank model, which is commonly used for the description of production processes,[30] can indeed satisfactorily predict the basic bifurcation scenarios. Universal features are established in terms of symbolic dynamics and iterated one-dimensional maps. The methods which work successfully in this case could be generalized to suit other systems as well.

This work is organized as follows. In Section 2 we study the generation and motion of single fronts. It turns out that two complementary types of fronts, namely the electron accumulation front, and the electron depletion front exist. We examine the velocity of single fronts as a function of the applied external current, and study the motion of multiple fronts, which is governed by the global constraint of the externally applied voltage. Particular consideration is given to the influence of the contact boundary conditions on the generation and annihilation processes of fronts.

In Section 3 we systematically study the dynamical behavior of the microscopic superlattice model at different voltages and boundary conditions numerically. Combining the results from Section 2 we derive a simplified front model, and corroborate its validity by comparing the resulting bifurcation scenarios with our previously obtained numerical data, in particular the scenarios leading to chaos under a fixed external voltage. Under the additional assumption that fronts do not traverse the whole system, we finally obtain in Section 4 a tank model, which explains the basic bifurcations by a set of filling rules for a system of water tanks. In the most simple nontrivial case this system further reduces to a one-dimensional map, which can be analyzed analytically in terms of the universal U-sequence for unimodal one-dimensional maps.

2. FRONT DYNAMICS IN ONE SPATIAL DIMENSION

In a weakly coupled semiconductor superlattice with a large number of quantum wells, charge accumulation and depletion fronts typically occur, and play a major role in the dynamical behavior of the system. Such fronts are either stationary or move with positive or negative velocities. Particularly interesting scenarios may arise if fronts of opposite polarity collide and annihilate (see Fig. 1). In this section we will discuss the basic dynamics of fronts in detail.

Our analysis starts from a well known microscopic sequential tunneling model which is explained in detail in ref. 22, and also reviewed in ref. 23. The dynamical variables of this model are the two-dimensional electron densities n_m of each well m of the superlattice, which evolve according to the continuity equation,

$$e\dot{n}_m = j_{m-1\to m} - j_{m\to m+1} \quad \text{for } m = 1, \ldots, N. \tag{1}$$

Here $e < 0$ is the charge of the electron, N is the number of wells in the superlattice, and $j_{m\to m+1} = j_{m\to m+1}(F_m, n_m, n_{m+1})$ is the current density from well m to well $m+1$, which depends on the electric field F_m between these two wells, and the respective electron densities n_m and n_{m+1}. The electric fields F_m are connected to the electron densities n_m by a discrete version of Gauss's law:

$$\epsilon_r \epsilon_0 (F_m - F_{m-1}) = e(n_m - N_D) \quad \text{for } m = 1, \ldots, N. \tag{2}$$

The external applied voltage imposes a global constraint:

$$U = -\sum_{m=0}^{N} F_m d. \tag{3}$$

Here ϵ_r and ϵ_0 are the relative and absolute permittivities, d is the period of the superlattice, and N_D is the two-dimensional doping density. The explicit form of the nonlinear function $j_{m\to m+1}(F_m, n_m, n_{m+1})$ is derived from microscopic considerations.[22] In the case $n_m = n_{m+1} = N_D$ the current density vs electric field characteristic is shown in Fig. 2. For the current densities at the contacts we use the following simple Ohmic boundary current densities:[31]

$$j_{0\to 1} = \sigma F_0, \tag{4}$$

$$j_{N\to N+1} = \sigma F_N \frac{n_N}{N_D}. \tag{5}$$

where σ is the Ohmic conductivity, and the factor n_N/N_D is introduced in order to avoid negative electron densities at the collector.

In the following we will assume a superlattice consisting of $N = 100$ periods with $w = 8.0\,\text{nm}$ wide GaAs wells and $b = 5.0\,\text{nm}$ wide $Al_{0.3}Ga_{0.7}As$ barriers at $T = 20K$ and a doping density of $N_D = 10^{11}\,\text{cm}^{-2}$. Two examples for the evolution of the electron densities, electric fields and currents are shown in Fig. 3.

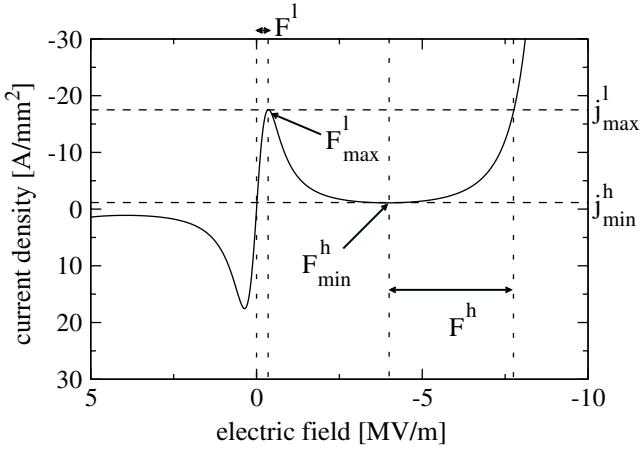

Fig. 2. Homogeneous well-to-well current density vs. field characteristic. F^l and F^h denote the low and high-field region on the first and third branch of the characteristic, respectively. The transition from the first branch to the second branch occurs at $(F^l_{\max}, j^l_{\max}) = (-0.36\,\mathrm{MV/m},\ -17.6\,\mathrm{A/mm^2})$ and the transition from the second to the third branch at $(F^h_{\min}, j^h_{\min}) = (-3.95\,\mathrm{MV/m}, -1.10\,\mathrm{A/mm^2})$. Only the second branch exhibits negative differential conductivity.

2.1. Dynamics of a Single Front

The dynamics of single fronts in discrete systems have been extensively studied in various contexts,[32–35] including the specific case of semiconductor superlattices.[22,36–39] Although the general theory of front propagation in discrete systems tends to become rather complicated,[35] we will show that the basic properties of fronts in semiconductor superlattices can be understood easily by considering the "operating points" on the current density vs. electric field characteristic across each barrier.

Let us first consider the case of a single charge accumulation front, which is located far away from the contacts. This front is characterized by a number of consecutive quantum wells with indices $m_l, \ldots, m_r$, where the electron densities are noticeably larger than the doping density N_D, whereas outside of the front the electron densities are approximately equal to N_D, i.e.

$$n_m > N_D + 5\% \quad \text{for } m \in [m_l, m_r], \tag{6}$$

$$n_m = N_D \pm 5\% \quad \text{else .} \tag{7}$$

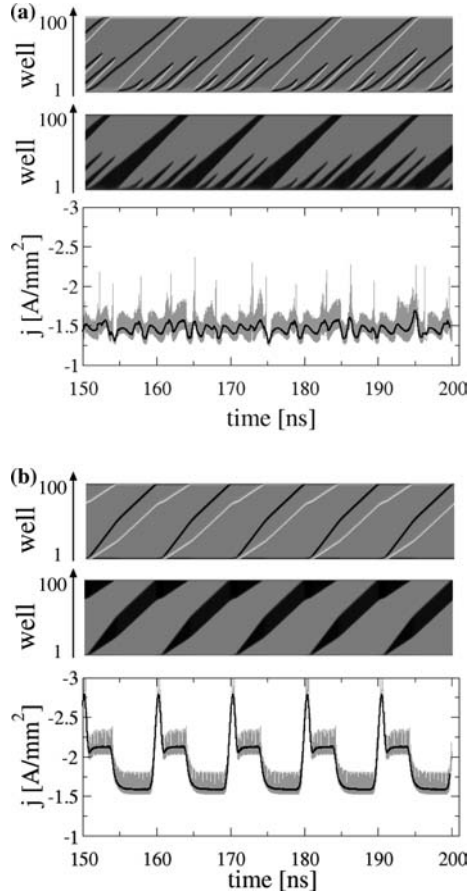

Fig. 3. Examples for the evolution of the electron densities (top panels), electric fields (middle panels) and current densities (bottom panels) of the superlattice for an external voltage $U = 2\,\mathrm{V}$ and contact conductivity $\sigma = 0.5\,\Omega^{-1}\mathrm{m}^{-1}$ (a) and $\sigma = 1.3\,\Omega^{-1}\mathrm{m}^{-1}$ (b). In the top panels the electron accumulation and depletion layers are shaded in white and black, respectively. The black areas in the middle panels show the high field domains. The current density in the lower panels is plotted in gray, while the black lines show a running average of the current over an interval of 0.5 ns.

Here a heuristic 5% accuracy cutoff is introduced since even far away from the front the electron density is never *exactly* equal to the doping density. An analogous definition for m_l and m_r applies in the case of a charge depletion front.

Instead of fixing the voltage drop U at the device by (3), it turns out to be advantageous to study the front motion at a fixed current density[19]

$$j = \frac{1}{N+1} \sum_{m=0}^{N} j_{m \to m+1} \tag{8}$$

instead (here we neglected any contributions from the displacement current (internal capacitance), since we are interested in the current inside the sample). Practically this is achieved by introducing a large external series resistor R, and setting

$$-U = -U_0 - RAj, \tag{9}$$

where A is the sample cross section, and U_0 is the fixed overall voltage. For a sufficiently large R we have $|U| \ll |RAj|$. The current density is then approximately fixed by

$$-j = \frac{U_0}{RA} - \frac{U}{RA} \approx \frac{U_0}{RA}. \tag{10}$$

Note that U itself is not assumed to be fixed. However, a change in U due to the internal degrees of freedom of the superlattice will only have a tiny effect on j, according to (10).

A typical profile for the electron density and the electric field of an electron accumulation front under fixed current density conditions is shown in Fig. 4. In this case the front width is about six wells.

Far away from the front, the well-to-well current densities obey the homogeneous current density vs. field characteristic as in Fig. 2. Furthermore the electric field must be located on one of the branches with positive differential conductivity, since otherwise the configuration would not be stable against small charge fluctuations. For a fixed current density, this determines the low and high fields $F^l(j)$ and $F^h(j)$, respectively (see Fig 2). The field obeys Gauss's law (2) and therefore increases[3] from $F^l \approx 0$ to a large negative value F^h with increasing well number m. The total

[3]Due to the negative sign of the electron, the electric fields and current densities are negative for our choice of the coordinate system. It is nevertheless customary to call F^h the *high* field and F^l the *low* field, although formally $0 > F^l > F^h$. Consequently, terms like *increasing* and *decreasing* are used in reversed logic in connection with fields and current densities.

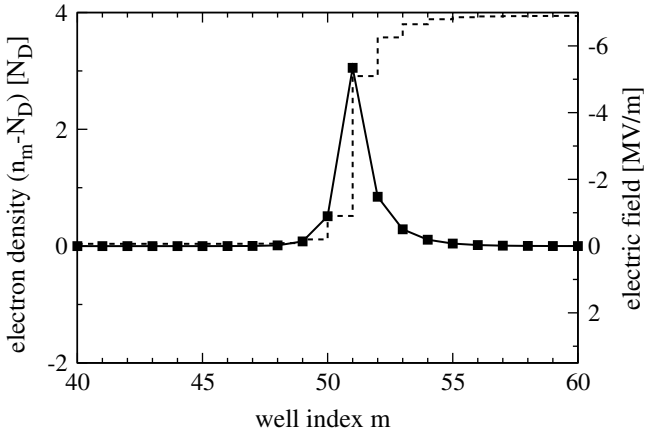

Fig. 4. Electron density (full line) and electric field (dotted) profile for a stationary charge accumulation front at constant current density $j = -6.0\,\mathrm{A/mm^2}$.

charge $Q_a < 0$ per unit area in the accumulation front is then simply given by

$$Q_a(j) = \sum_{m=m_l}^{m_r} e(n_m - N_D) = \epsilon_r \epsilon_0 (F^h(j) - F^l(j)). \tag{11}$$

Here we assume that the current is fixed to the same value at both sides of the front, which is only possible if the current density is chosen in the interval where the multistability in the field occurs (cf. Fig. 2). Otherwise Q_a would be time-dependent, and the front would be unstable.

In the case of an electron depletion front, the electron density and field profiles are shown in Fig. 5. The electric field shows a drop from $F^h(j)$ to $F^l(j)$ with increasing well index m. By comparing with (11) it is obvious that the total charge of the depletion front is $Q_d = -Q_a$. We furthermore note that the charge profile of the depletion front is flatter and broader than for the accumulation front. The reason for this difference is that the electron density n_m is required to be positive. Therefore, the contribution of one well to the total charge Q_d can not exceed $-eN_D$. Such a restriction does not apply for charge accumulation fronts, since there is no upper limit on n_m. In fact we see from Fig. 4 that for this choice of parameters, the majority of the charge in an accumulation front is located within one single well.

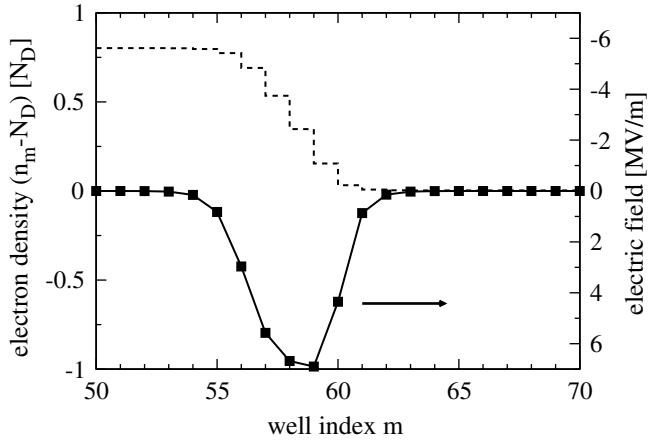

Fig. 5. Electron density (full line) and electric field (dotted) profile for a charge depletion front moving with positive velocity at a constant current density $j = -2.0\,\mathrm{A/mm^2}$.

2.1.1. The Current–Velocity Characteristic

In order to study the motion of charge fronts it is useful to define the position $p_{a/d}$ of the electron accumulation or depletion front by its center of charge,

$$p_{a/d} = \sum_{m=m_l}^{m_r} md \frac{e(n_m - N_D)}{Q_{a/d}}. \tag{12}$$

Note that $p_{a/d}$ is a real number, although the underlying superlattice is discrete. The velocity $v_{a/d}$ of an accumulation or depletion front can then be obtained by differentiating (12) with respect to time and using the continuity equation (1)

$$v_{a/d} = \dot{p}_{a/d} = \sum_{m=m_l}^{m_r} md \frac{j_{m-1\to m} - j_{m\to m+1}}{Q_{a/d}} \tag{13}$$

$$= \frac{d}{Q_{a/d}} \left(m_l j_{m_l-1\to m_l} + \sum_{m=m_l}^{m_r-1} j_{m\to m+1} - m_r j_{m_r\to m_r+1} \right) \tag{14}$$

$$\approx \frac{d}{Q_{a/d}} \sum_{m=m_l}^{m_r-1} \left(j_{m\to m+1} - j \right), \tag{15}$$

where in the last step we have used that $j_{m_l-1\to m_l} \approx j_{m_r\to m_r+1} \approx j$, which is fulfilled to a high degree of accuracy for all current densities outside the front as defined by (6).

Further insight into the term $j_{m\to m+1} - j$ appearing in (15) can be gained by differentiating Gauss's law (2) with respect to t and using the continuity equation (1). This yields

$$\epsilon_r\epsilon_0\dot{F}_m + j_{m\to m+1} = \epsilon_r\epsilon_0\dot{F}_{m-1} + j_{m-1\to m} \quad \text{for } m = 1,\ldots,N, \tag{16}$$

which by induction over m gives

$$\text{const} = \epsilon_r\epsilon_0\dot{F}_m + j_{m\to m+1} \quad \text{for } m = 0,\ldots,N, \tag{17}$$

where the left-hand side of (17) does not depend on m. For $m \notin [m_l, m_r]$ we have $\dot{F}_m = 0$ and $j_{m\to m+1} = j$, which yields const $= j$, and therefore

$$\epsilon_r\epsilon_0\frac{\mathrm{d}F_m}{\mathrm{d}t} = j - j_{m\to m+1} \quad \text{for } m = 0,\ldots,N. \tag{18}$$

Using (18) together with (2) and (3) leads to an alternative set of dynamical model equations in terms of electric fields, instead of electron densities, which is well studied in the literature.[40,41]

Substituting (18) into (15) and using the fact that $\dot{F}_m = 0$ for $m \notin [m_l, m_r]$ we obtain

$$v_{a/d} = -\frac{d}{Q_{a/d}}\sum_{m=0}^{N}\epsilon_r\epsilon_0\frac{\mathrm{d}F_m}{\mathrm{d}t}. \tag{19}$$

Using (3) and (11) finally yields the simple relation

$$v_{a/d} = \pm\frac{1}{F^h(j) - F^l(j)}\frac{\mathrm{d}U}{\mathrm{d}t}. \tag{20}$$

We may use (20) to obtain the front velocities as a function of j numerically. For this purpose, we approximately fix the current density j using a large load resistor ($RA = 10^9\,\Omega\,\mathrm{m}^2$) according to (10). We then calculate the slope of the sample voltage $U(t)$ by numerical regression. The corresponding results are shown in Fig. 6. For the depletion front (solid line in Fig. 6) we obtain an always positive velocity which is approximately proportional to the current density. For small current densities however the depletion front becomes unstable (dotted line) which is due to the fact

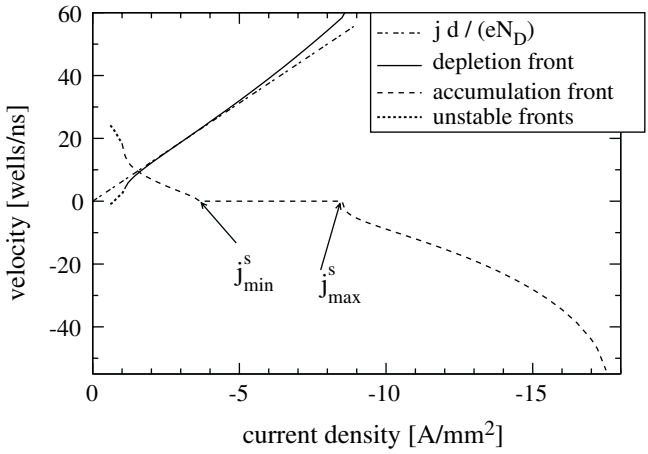

Fig. 6. Front velocity vs. current density for electron accumulation and depletion fronts of superlattice B. The dotted lines denote unstable fronts. $j^s_{\min}$ and $j^s_{\max}$ denote the minimum and maximum current for the stationary accumulation front. The dash-dotted line is the analytical prediction of the depletion front velocity according to (21).

that the high field branch $F^h(j)$ of the homogeneous current density characteristic can not support arbitrarily small currents, but has a minimum at $j^h_{\min} \approx -1.15\,\mathrm{A/mm^2}$ (see Fig. 2). If we try to impose an external current density below $j^h_{\min}$, this will only affect the low field region, which is at the right of the front. Consequently more electrons are entering the front from the left than are leaving at the right border, until the depletion front has vanished.

For the electron accumulation front (dashed line in Fig. 6) the velocity vs. current density characteristic is more complicated. For small currents the front is unstable for the same reasons as the depletion front above. With increasing current the velocity drops from positive values to zero, which means that the front becomes stationary. The fact that the front can be *pinned* for a finite range of j is due to the discreteness of our system, and would disappear in the continuous limit $N \to \infty$, $d \to 0$. With further increase of the current, the front is unpinned and starts to move with negative velocity, i.e upstream towards the emitter.[37] Since currents larger than $j^l_{\max} \approx -17.5\,\mathrm{A/mm^2}$ are not supported by the low-field branch of the homogeneous characteristic (Fig. 2), the accumulation fronts become unstable beyond $j^l_{\max}$.

2.1.2. Depletion Front with Positive Velocity

The simplest case of front propagation is that of a depletion front (Fig. 5). For $m \in [m_l, m_r]$ the current density vs. electric field characteristic

$j_{m\to m+1}(F, n_m, n_{m+1})$ will not simply obey the homogeneous characteristic of Fig. 2, since n_m and n_{m+1} are different from N_D. But if the electron density profile n_m is known for one particular front, we can calculate the inhomogeneous characteristic $j_{m\to m+1}(F, n_m, n_{m+1})$ as a function of F at each m separately.

The resulting current density characteristics are shown in Fig. 7. We see that at the left and right borders of the front we obtain an almost homogeneous characteristic (dashed and dotted lines in Fig. 7), since there the electron densities are not too different from the doping density. Inside the front the electron concentration is depleted and almost vanishes at the center of the front (see well 58 and 59 in Fig. 5). This results in severely suppressed current density characteristics (dash-dotted line in Fig. 7), which are in particular below the external current j (solid line) for any field between F^l and F^h.

Let us now consider the operating points $(F_m, j_{m\to m+1})$. At the left boundary of the front the operating point is close to $(F^h(j), j)$ $((F_{55}, j_{55\to 56})$ in Fig. 7). With increasing well index m the field F_m decreases towards F^l and the current $j_{m\to m+1}$ drops to almost zero and rises again to j. We therefore note that all contributions to the velocity in (15) are positive, and we conclude $v_d > 0$.

A useful approximation for the velocity v_d can be obtained by considering (18) at the center of the front, where we can approximate $n_m \approx 0$.

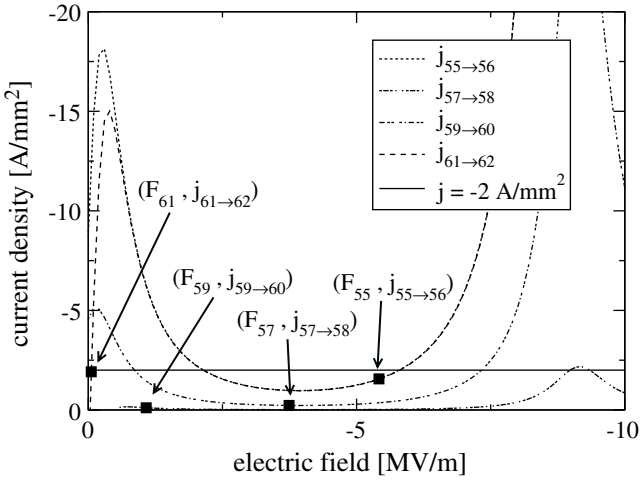

Fig. 7. Various well-to-well characteristics $j_{m\to m+1}(F, n_m, n_{m+1})$ for the charge depletion front of Fig. 5 at $j = -2\,\mathrm{A/mm^2}$. The black squares denote the actual operating points $(F_m, j_{m\to m+1}(F_m, n_m, n_{m+1}))$ if the field profile of Fig. 5 is taken into account.

Then we have $j_{m\to m+1}=0$, and $\dot{F}_m = j/(\epsilon_r\epsilon_0)$. From Gauss's law (2) we know on the other hand that $F_{m-1}=F_m+eN_D/(\epsilon_r\epsilon_0)$. The time Δt at which $F_m(t+\Delta t)=F_{m-1}(t)$ is then given by $\Delta t = eN_D/j$. But Δt is also the time needed for the front to travel by one well period d. Thus the velocity of the depletion front is positive and can be approximated by[38,36]

$$v_d \approx \frac{jd}{eN_D}. \tag{21}$$

From Fig. 6 we see that this approximation is in very good agreement with the numerical calculations, except for current densities close to the front instability. However, we stress that (21) is only valid for rather low doping density, i.e. $-eN_D < Q_d$ since the derivation depends on the presence of at least one completely depleted well with $n_m \approx 0$. It was in fact shown by Wacker[22] that for high doping values even negative velocities for v_d are possible.

2.1.3. Stationary Accumulation Front

Let us now consider a stationary accumulation front, i.e $\partial_t n_m = 0$ for all m at a fixed external current density j (cf. Fig. 4). Let us denote by m_p the well with the highest electron concentration (for Fig. 4 we have $m_p = 51$). The individual well-to-well characteristics close to m_p are shown in Fig. 8.

We see that by approaching the front from the emitter side, we first observe an almost homogeneous characteristic (dotted line in Fig. 8) and a current density electric field operating point close to (F^l, j) (diamond). But already at the next barrier the current density characteristic $j_{m_p-1\to m_p}(F)$ (double dot dashed line) shows a suppressed low field peak. This is due to the large electron concentration at well m_p inhibiting the tunneling of electrons into well m_p. Since the electric fields are constant in time, we conclude from (18) that in particular $j_{m_p-1\to m_p}=j$, while the electric field F_{m_p-1} is larger than F^l (black square). At the next barrier the current density takes advantage of the large electron density n_{m_p}, which yields a characteristic $j_{m_p\to m_p+1}(F)$ (dashed line). The electric field F_{m_p} (circle) has increased by a large amount due to $n_{m_p} > N_D$, but the current is fixed at $j_{m_p\to m_p+1}=j$. For even larger m the characteristic again approaches the homogeneous characteristic and the operating point is close to (F^h, j). Since at any barrier we have $j_{m_p\to m_p+1} = j$, the total velocity of the front is zero according to (15). Note that no

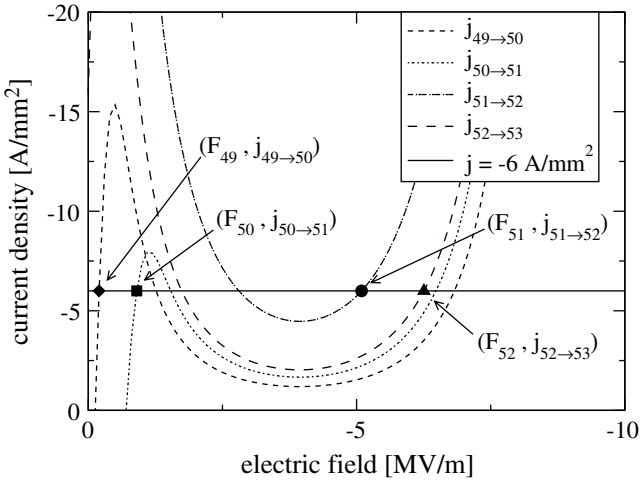

Fig. 8. Well-to-well characteristics as in Fig. 7, but for a stationary charge accumulation front at $j = -6.0\,\mathrm{A/mm^2}$. For the electric field and electron density profile of this front see Fig. 4.

operating point is located at the unstable branch with negative differential conductivity. This is only possible in a discrete system, where the field changes by a finite amount from one barrier to the next. It thus follows that stationary fronts of this type can not appear in a continuous system, since there the branch with negative differential conductivity can not be avoided.

2.1.4. Accumulation Front with Positive Velocity

By lowering the external current j we arrive at well-to-well characteristics as in Fig. 9. By comparing with Fig. 8 we note that the characteristics themselves did not change considerably, but only the imposed external current j (solid line) is lowered. In particular there is now no operating point, at which the characteristic $j_{m_p\to m_p+1}(F)$ could assume j, i.e the dash-dotted characteristic and the solid line in Fig. 10 do not intersect. Instead we have $j_{m_p\to m_p+1}(F_{m_p}) < j$, which results in a positive velocity by (15). An analytical approximation for this velocity is given in ref. 42.

2.1.5. Accumulation Front with Negative Velocity

Besides positive and zero velocities, the electron accumulation fronts show negative velocities for external currents larger than j^s_{max} (see Fig. 6).[37]

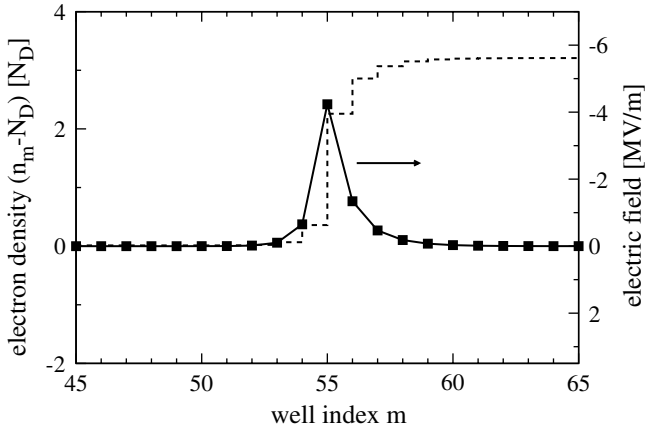

Fig. 9. Electron density (full line) and electric field (dotted) profile for a charge accumulation front moving in positive direction at constant current $j = -2.0\,\mathrm{A/mm^2}$.

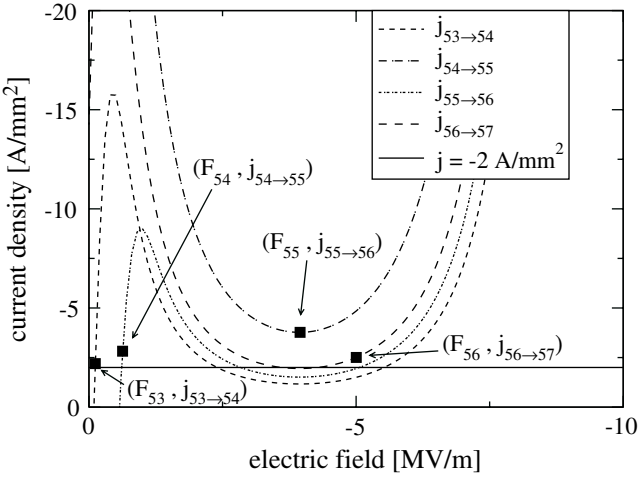

Fig. 10. Well-to-well characteristics for a right moving charge accumulation front at $j = -2.0\,\mathrm{A/mm^2}$ (profile in Fig. 9).

For a charge accumulation front moving left, the charge and field profiles (Fig. 11) are very similar to the stationary case (Fig. 4). Consequently the well to well characteristics in Fig. 12 are also similar to the stationary ones (Fig. 8) but with an external current j (horizontal solid line in Fig. 12) at a higher value. Due to this rise of j there is now no intersection point of the characteristic $j_{m_p-1\to m_p}(F)$ (dash double dot-

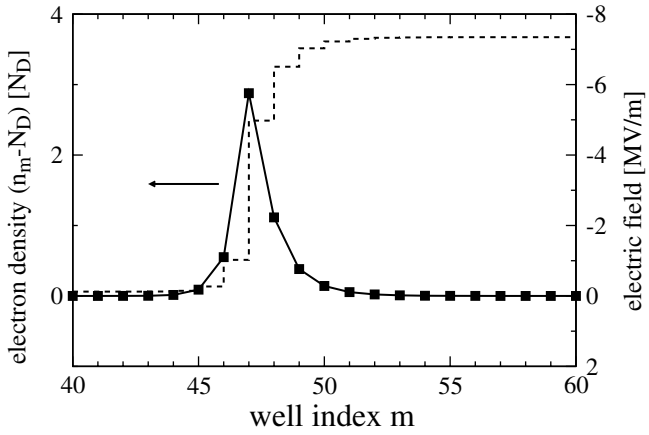

Fig. 11. Electron density (full line) and electric field (dotted) profile for a charge accumulation front moving in negative direction at constant current $j = -10.0\,\mathrm{A/mm^2}$.

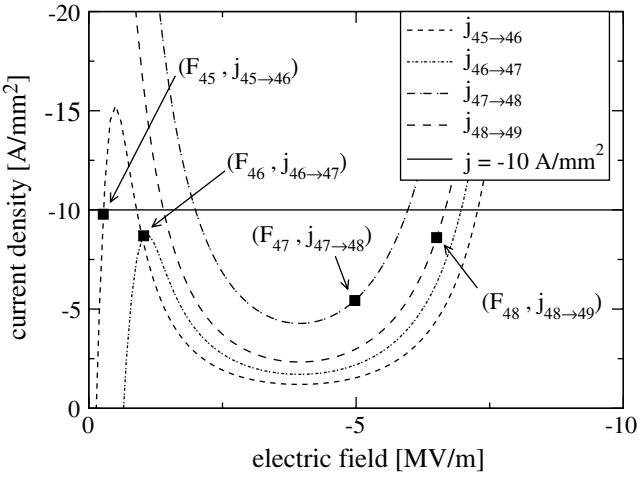

Fig. 12. Well-to-well characteristics for the left moving charge accumulation front in Fig. 11.

ted line) with j on the first branch. This means that the operating point $(F_{46}, j_{46\to47})$ is below j and results in a negative contribution in (15). Since all other operating points are also less than or equal too j, we conclude that v_d in this regime will be negative.

2.2. Multiple Fronts under Fixed External Voltage

In the previous section we have studied the motion of a single front at fixed external current j far away from the contact and obtained the front velocity vs. current density characteristic in Fig. 6. We now consider the case of several fronts, which are assumed to be well separated and far away from the contacts. Instead of fixing j we now fix the external voltage U, which is experimentally much more convenient.

Since the fronts are assumed to be separated, the indices m_l and m_r in (12) are well defined for each individual front, and we may therefore calculate the positions of each accumulation front $a_1 \dots a_{N_a}$ and depletion front $d_1 \dots d_{N_d}$. Here N_a and N_d are the number of accumulation and depletion fronts, respectively. Since accumulation and depletion fronts appear alternatingly in the vertical direction, we have

$$N_a - N_d = +1, 0, -1. \tag{22}$$

Let us define by

$$L_h(j) = \frac{-U - LF^l(j)}{F^h(j) - F^l(j)} \approx \frac{-U}{F^h(j)} \tag{23}$$

the partial length of the superlattice which is in the high-field regime. Here $L = Nd$ is the total length of the superlattice, and in the last step we have used the approximation $F^l \approx 0$. From (12) and (3) it follows that L_h imposes a global constraint on the front positions by

$$L_h(j) = \sum_{i=1}^{N_d} d_i - \sum_{i=1}^{N_a} a_i \mod L. \tag{24}$$

The expression mod L in (24) means that L has to be added if $a_{N_a} > d_{N_a}$ such that $L_h \in [0, L]$. We stress that due to our center-of-mass-like definition of the front positions, (24) is exact, even for fronts with a finite width. In particular, the discreteness of the superlattice does not play a role here.

Differentiating (23) and (24) with respect to t for $U = \text{const}$ yields

$$\frac{\partial L_h}{\partial t} = \frac{U}{\left(F^h\right)^2} \frac{\partial F^h}{\partial j} \frac{\partial j}{\partial t} \tag{25}$$

and (using (13))

$$\frac{\partial L_h}{\partial t} = N_d v_d - N_a v_a, \tag{26}$$

respectively. By combining (25) and (26) we obtain the evolution equation for the current density,

$$\frac{\partial j}{\partial t} = (N_d v_d(j) - N_a v_a(j)) \frac{\left[F^h(j)\right]^2}{U \frac{\partial F^h}{\partial j}}. \tag{27}$$

Similar relations were derived for various front systems,[23] e.g. continuous drift-diffusion systems describing space-charge waves in extrinsic p-Ge bulk semiconductors[20] or n-GaAs Gunn diodes.[43] As stated before, (27) holds only if the fronts are well separated from each other and in particular the length of the device is much larger than the width of the fronts as discussed in more detail in ref. 23. In this limit conditions under which a front dynamics based on (27) may describe a generic system for the Gunn instability have been derived in ref. 21.

From (27) it follows that the current will relax to a state where the important relation

$$N_a v_a(j) = N_d v_d(j). \tag{28}$$

holds.

From the denominator in (27) we note that this relaxation will be fast, if U and $(\partial F^h/\partial j)$ are small. For example we may consider the relaxation towards the dipole domain current density j_d with $N_d = N_a = 1$. In linear approximation we have

$$v_{a/d}(j) \approx v_{a/d}(j_d) + (j - j_d)\partial_j v_{a/d}(j_d). \tag{29}$$

From (21) we obtain $\partial_j v_d = d/(eN_D)$. From Fig. 13 we may further approximate (for this particular superlattice only) $\partial_j v_a(j_d) \approx -\partial_j v_d(j_d)$. Using $v_a(j_d) = v_d(j_d)$ we get for the first factor in (27),

$$(N_d v_d(j) - N_a v_a(j)) \approx (j - j_d)\left(\partial_j v_d(j_d) - \partial_j v_a(j_d)\right) \approx (j - j_d)\frac{2d}{eN_D}. \tag{30}$$

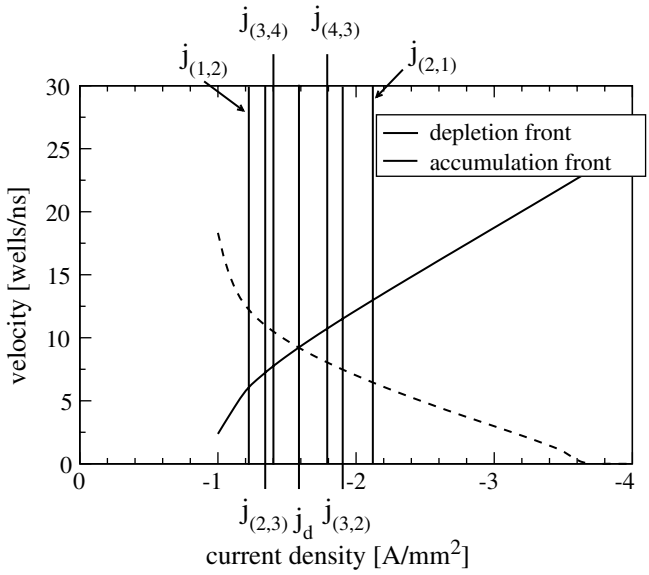

Fig. 13. Velocity vs. current density characteristic as in Fig. 6, in the region around j_d, where the accumulation and depletion front velocities are equal. $j_{(N_a,N_d)}$ denote the points where $N_a v_a = N_d v_d$ (cf. (28)), respectively.

Since this factor vanishes at $j = j_d$, the leading contribution from the second factor in (27) is in zeroth order of $(j - j_d)$. Using (23) we arrive at

$$\frac{1}{j_d}\frac{\partial j}{\partial t} \approx -\frac{j - j_d}{j_d}\frac{2d}{eN_D}\frac{F^h(j_d)}{L_h \partial_j F^h(j_d)} \approx -\frac{j - j_d}{j_d}\frac{d}{L_h}\frac{1}{\tau_{\text{eff}}} \tag{31}$$

with $\tau_{\text{eff}} \approx 1\,\text{ps}$. Since $L_h/d < N$, which is the number of wells in the high field domain, we obtain typical relaxation times of less than 100 ps. During this time, the fronts typically travel less than two wells, which justifies the simplification that the current relaxation according to (31) is almost instantaneous. This means that (28) is always immediately fulfilled, in the limit of well separated fronts.

If the number of fronts N_a and N_d is given, the current density j is fixed by (28). In the case $N_a = N_d$, i.e. an even number of fronts, we have $j = j_d$, where j_d is at the intersection point of $v_a(j)$ and $v_d(j)$, see Fig. 13. Similarly for the tripole configuration consisting of two accumulation fronts and one depletion front, the current density $j = j_{(2,1)}$ is fixed by $2v_a(j_t) = v_d(j_t)$. For other configurations the corresponding current densities are described in Fig. 13. Since there is only a countable set

of configurations, the set of possible j is discrete with j_d being the only limit point.

With this knowledge we can now explain the current density trace of Fig. 3(b), which alternates between a dipole and a tripole configuration. For a dipole configuration with one accumulation and one depletion front, the averaged current density is fixed to the constant value j_d, while in the tripole configuration with two depletion and one accumulation fronts, we obtain $j = j_{(2,1)}$ as predicted from (28). In this context it is instructive to realize the meaning of (28) directly from the field evolution (middle panel of Fig. 3(b)) in the tripole phase. Due to the fixed voltage, the total length of the high-field domain is required to be constant. Since the high-field domain shrinks with the motion of the two accumulation fronts and increases by the depletion front, the velocity of the depletion front obviously has to be twice the velocity of the accumulation fronts.

In contrast to the averaged current density, the current density trace (gray line in Fig. 3(b)) shows rapid spikes which are due to the discreteness of the superlattice[44] (well-to-well hopping of charge packets, cf. ref. 45).

In the current density trace of Fig. 3(a) we also observe plateaus corresponding to the currents density $j_{(1,2)}$, $j_{(2,3)}$, $j_{(3,4)}$ and j_d, although they are not as flat and well developed as in Fig. 3(b). The reason for this difference will become clearer in Section 3.

2.3. Front Generation and Annihilation

So far we have only considered the free motion of charge fronts well separated from each other and the contacts. But for interesting dynamical scenarios as for example in Fig. 3(a), we also need front generation and front annihilation processes.

2.3.1. Front Collisions

From the current-velocity characteristic Fig. 13 and from (28) we conclude that the accumulation and depletion fronts may move at different velocities. This opens up the possibility for a collision of two fronts with opposite polarity, and may lead to interesting scenarios. Such a collision is shown in Fig. 14. We see that both fronts annihilate each other, as can be expected from the fact that $Q_a = -Q_d$.

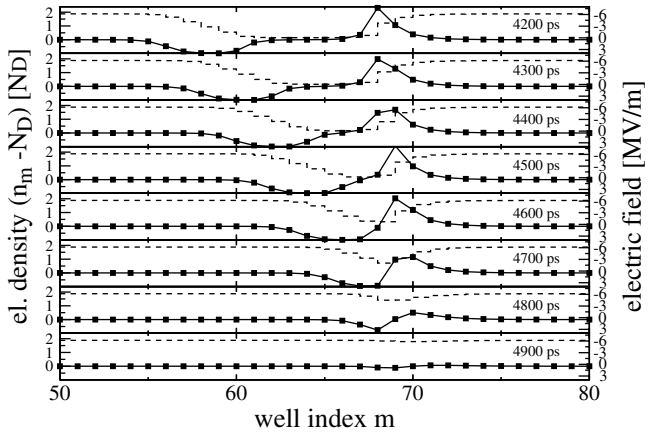

Fig. 14. Electron density (full lines) and electric field profiles (dotted lines) for a collision and annihilation process of a fast depletion front with a slow accumulation front. Parameters: $\sigma = 1\,\Omega^{-1}\mathrm{m}^{-1}$; $j = -3\,\mathrm{A/mm}^2$.

2.3.2. Front Annihilation at the Collector

A further rather unspectacular elementary process is a front reaching the collector. Such a front gets absorbed by the contact and vanishes from the system (cf. Fig. 3), thereby reducing N_a or N_d by one.

2.3.3. Front Injection at the Emitter

In the superlattices under consideration, both types of fronts are in general only generated at the emitter. We will see that the choice of the boundary conditions, as well as the imposed external current j play a decisive role for the front generation. For convenience we assume that the emitter contact is Ohmic (4),

$$j_{0\to 1}(F_0) = \sigma F_0 \tag{32}$$

with σ the contact conductivity, and F_0 the electric field between the emitter and the first well. In the following we will choose σ such that the linear contact characteristic $j_{0\to 1}(F_0)$ intersects the N-shaped homogeneous characteristic $j_{1\to 2}(F_1, N_D, N_D)$ at a point (F_c, j_c) on its branch with negative differential conductivity (see Fig. 15).

Let us consider a superlattice under fixed external current density j, with initial conditions

$$n_i(t=0) = N_D, \quad F_0(t=0) = j/\sigma. \tag{33}$$

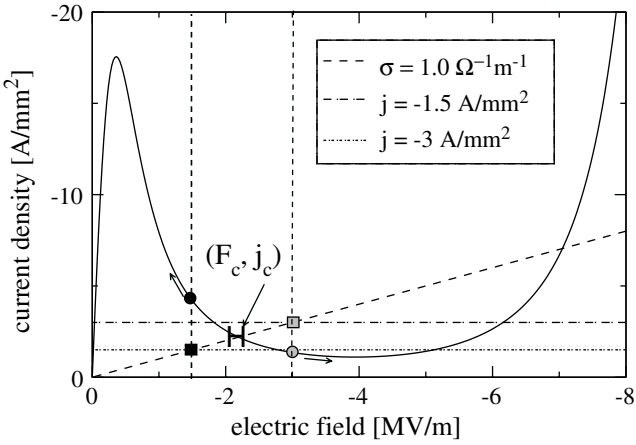

Fig. 15. Emitter current density characteristic compared to homogeneous well to well characteristic $j_{m\to m+1}(F, N_D, N_D)$. The intersection point of the two characteristics is denoted by (F_c, j_c).

It follows from (18) that F_0 is a stable fixed point. From (2) we see that $F_1(t=0) = F_0$. Let us first assume that j is larger than j_c (double dot dashed horizontal line in Fig. 15). In this case F_0 and $F_1(t=0)$ are larger than F_c (shaded square and shaded circle in Fig. 15), which means that

$$|j_{1\to 2}| < |j_c| < |j| = |j_{0\to 1}|. \tag{34}$$

Consequently, $F_1(t)$ will *increase* towards higher values due to (18) until it eventually reaches $F_1 \approx F^h(j)$.[4] If on the other hand j is smaller than j_c (dot dashed line in Fig. 15) $F_1(t)$ will *decrease* for complementary reasons (black circle). It is now apparent that the choice of the external current j in comparison to the intersection point j_c is crucial. From the above discussion we come to the conclusions that

$$|j| > |j_c| \Rightarrow \text{ high field at emitter, i.e. } F_1(t \gg 0) \approx F^h(j), \tag{35}$$

$$|j| < |j_c| \Rightarrow \text{ low field at emitter, i.e. } F_1(t \gg 0) \approx F^l(j). \tag{36}$$

We may now argue that (35) and (36) are still approximately valid, even if the initial conditions (33) are not fulfilled. Let us consider a

[4] F_1 is not exactly equal to $F^h(j)$, since for $t > 0$ we have $n_1 > N_D$. Therefore, $j_{1\to 2}$ does not obey the homogeneous characteristic and its high-field intersection point with the external current j will be between $F^h_{\min}$ and $F^h(j)$.

superlattice at a fixed external current j, which initially contains an accumulation front at a position p_a far away from the boundary, and possibly further fronts at positions $p > p_a$. Then the region to the left of p_a including the emitter region is in the low field domain. If j is larger than j_c the emitter region is required to be at a high field by (35). This apparent "conflict" can be resolved by the dynamic generation of a new charge depletion front at the emitter. A converse argument applies for the generation of an accumulation front. The preliminary rules for the front generation can therefore be summarized by

GI Generate accumulation front at emitter, if $|j| < |j_c|$ and if the leftmost front is a depletion front.

GII Generate depletion front at emitter, if $|j| > |j_c|$ and if the leftmost front is an accumulation front.

In Fig. 16 we checked numerically that the approximations leading to rules GI, GII are justified, by examining the front generation for different values of j and σ. We see that the conditions for depletion front generation can be accurately predicted by GII. In the case of the generation of accumulation fronts, GI can only be checked for currents $|j| < |j^s_{\min}|$ (Fig. 6), since otherwise the newly generated front has zero or negative velocity and will not detach from the emitter.

Rules GI, GII only apply if the leftmost front is already fully detached from the emitter. Otherwise the newly generated front can anni-

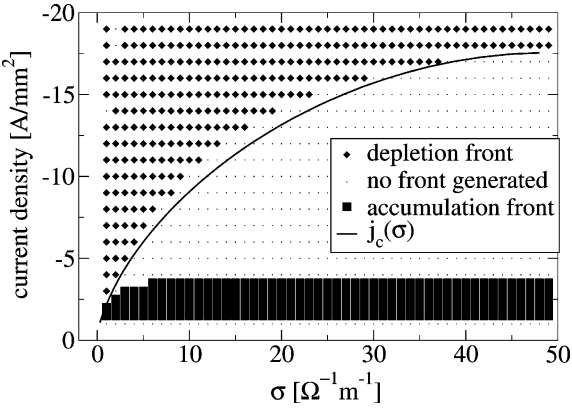

Fig. 16. Intersection point of the homogeneous characteristic with the emitter characteristic $j_c(\sigma)$. The diamonds and squares denote the successful generation of a depletion or accumulation front at the emitter.

hilate a nearby front of opposite polarity. This may occur in the common scenario of a dipole injection. Numerically we find, that the conditions of rule GII have to be fulfilled for a time interval of about 50 ps, before a depletion front to be fully developed. If the external current is switched, to the conditions given in rule GI before the depletion front is fully developed, the half formed depletion front retracts to the emitter contact.

The rule GI for the generation of an accumulation front should therefore be modified, to require that the leftmost depletion front is at least $p_h \approx 2d$ away from the emitter and a similar parameter p_l should be introduced into GII. The revised rules for front generation at the emitter then read:

GI′ Generate accumulation front at emitter, if $|j| < |j_c|$ and of the leftmost front is a depletion front which is at least at position p_h.

GII′ Generate depletion front at emitter, if $|j| > |j_c|$ and if the leftmost front is an accumulation front which is at least at position p_l.

We may now reexamine the scenario in Fig. 3(b). At $t = 157$ ns we have a dipole configuration with a leading depletion and a trailing accumulation front. The current is therefore $j = j_d$. At $t = 160$ ns the depletion front reaches the collector, i.e. $N_d = 0$. Then (28) requires that the velocity of the remaining accumulation front drops to zero, and at the same time the current rises sharply due to Fig. 13. Eventually we have $|j| > |j_c| = 2.6\,\mathrm{A/mm^2}$ and a depletion front is injected at the emitter by GII′. After that j starts to drop towards j_d, but as soon as $|j| < |j_c|$, and the depletion front has traveled by p_h, the conditions for GI′ are fulfilled, and a new accumulation front is injected at the emitter at $t = 161$ ns. All in all we see that the system responds to the event that the first depletion front hits the collector, by the generation of a dipole with a leading depletion and trailing accumulation front at the emitter. For the resulting tripole configuration, the current $j_{(2,1)}$ is required (see Fig. 13). Since $|j_{(2,1)}| < |j_c|$ and the leftmost front is an accumulation front, no new fronts will be generated (see GI′,GII′), and a current plateau with $j = j_{(2,1)}$ is maintained until the rightmost accumulation front hits the collector at $t = 163$ ns. The current then drops to j_d, but no new front is generated at the emitter, until the cycle starts over again with the next depletion front reaching the collector at $t = 170$ ns.

3. BIFURCATIONS IN INTERACTING FRONT SYSTEMS

In Section 2 we have studied the basic building blocks for the front dynamics in one spatial dimension. In this section we will examine how those elements can be combined to yield interesting bifurcation scenarios,

including chaos. While chaoticity in periodically driven superlattices has been extensively studied theoretically[46–50] and experimentally[51,52] we will concentrate on the question, how chaotic behavior can be obtained under fixed external voltage conditions.[25,53]

For a fundamental understanding of the underlying bifurcations we will introduce the *front model*, which retains the basic bifurcation structure, but is much easier to handle numerically and analytically.

3.1. Microscopic Bifurcation Scenarios

We now use the external voltage U and the contact conductivity σ as the bifurcation parameters. From the discussion in Section 2.3.3 we learned that σ governs the injection of fronts at the emitter contact via the critical current $j_c(\sigma)$ (Fig. 16). Since the resulting bifurcation scenarios are complicated, we will first study the particular case of $\sigma = 0.5\,(\Omega\mathrm{m})^{-1}$, and later consider the necessary modifications for general σ.

3.1.1. The Case $\sigma = 0.5\,(\Omega\mathrm{m})^{-1}$

For $\sigma = 0.5\,(\Omega\mathrm{m})^{-1}$ we have $|j_{(1,2)}| < |j_c(\sigma)| < |j_d|$ (cf. Fig. 13). If we vary the applied voltage U, we typically observe front patterns as in Fig. 1, which are reminiscent of the chaotic front dynamics in an extrinsic Gunn-like bulk semiconductor.[20] In ref. 20 a model using delay times, instead of the parameters p_h and p_l, was proposed. The bifurcation scenario of that model still remains to be studied in detail, and it would be interesting to see whether that model can also be described in terms of U-sequences, which will be introduced in Section 4.

For a small voltage ($U = 0.50\,\mathrm{V}$) we observe that the fronts are generated as dipoles at the emitter, with a leading accumulation and a trailing depletion front. The leading accumulation front catches up with the depletion front of the preceding dipole, and the two fronts merge and annihilate at exactly the same position in each cycle. With increasing U, we observe what appears to be a period doubling cascade, with two ($U = 0.70\,\mathrm{V}$ in Fig. 1) and four ($U = 0.82\,\mathrm{V}$) alternating positions where the front annihilation occurs. A further increase in the voltage yields irregular behavior ($U = 0.90\,\mathrm{V}$, $1.00\,\mathrm{V}$, $1.20\,\mathrm{V}$) interrupted by periodic windows ($U = 1.05\,\mathrm{V}$). For even higher voltages, the fronts may occasionally reach the collector, but even then the interchange between chaotic ($U = 1.80\,\mathrm{V}$) and periodic ($U = 2.40\,\mathrm{V}$) regimes persists. Note that this bifurcation scenario appears to be different from the chaotic bifurcation scenario in the continuous drift-diffusion model of space charge waves in extrinsic semiconductors (cf. Fig. 5 of ref. 20). In particular, in ref. 20 chaoticity is only demonstrated

in the regime where fronts still reach the collector, in contrast to our findings.

The chaotic behavior can also be observed in the experimentally accessible current trace, as demonstrated in Fig. 17. Here we observe a further interesting feature, namely that not all fronts are *fully developed*. One example can be seen at $t = 155\,\text{ns}$ in the electron density plot of Fig. 17 (see also the case $U = 1.2\,V$ in Fig. 1). Here an accumulation front seems to detach from the emitter, but instead of catching up with the leading depletion front, it merges with a new depletion front from the emitter, before either of the fronts can be considered as fully developed. Such compositions of partly developed fronts can not be described in the framework of single stable fronts, which was developed in Section 2. In particular they do not obey the current velocity characteristic of Fig. 13. Such composite front phenomena, resemble the excitons in solid-state physics, since they often appear in pairs without net charge, and form a bound state with limited life time. Their dynamics may be treated by a yet to be developed correlated front theory, which is however beyond the scope of the present work. In the following we will refer to this kind

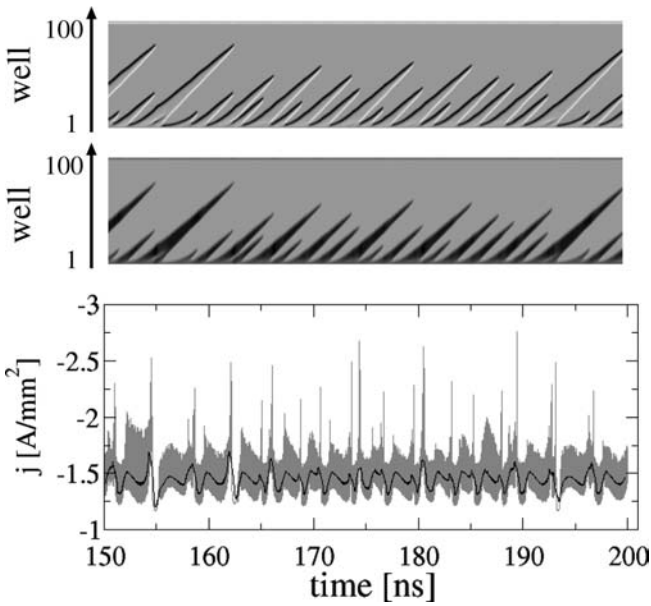

Fig. 17. Electron density (upper panel), electric field (middle panel) and current evolution (bottom panel) in the chaotic regime. Parameters as in Fig. 1, but with $U = 1.15\,\text{V}$. Same color code as in Fig. 3. The black current trace in the bottom panel is the running average of the raw current data (gray line) over an interval of 0.5 ns.

of phenomena as *excitonic* fronts. Similar effects also appear for pulses in excitable media.[54]

The difference between periodic and chaotic behavior is also illustrated by the phase portraits as shown in Fig. 18, which show the system trajectory in the phase space projected onto the subspace defined by n_{10} and n_{20}. In Fig. 18(a) the trajectory in the phase space is complicated, but still periodic, while in the chaotic regime in Fig. 18(b) the trajectory is aperiodic.

The full bifurcation scenario is shown in Fig. 19(a), where for each voltage U the set of front annihilation positions $\{p_c\}$ is plotted. Here we may interpret a discrete set of p_c's for a given voltage as an indication for periodic behavior (for instance the four points at $U = 0.82\,\mathrm{V}$, which correspond to a period four orbit), while a continuous set of collision points is an indication of chaotic behavior (cf. $U = 0.90\,\mathrm{V}$).

Starting from low voltages, we observe a period doubling bifurcation with periods 1, 2 and 4 in the regimes A, B, and C of Fig. 19(a), respectively. The following regime D contains two chaotic bands at its boundaries, which are separated by a period six orbit. While the chaotic band at the left edge of regime D is rather narrow, the band at the right edge is comparatively broad. The most striking feature in regime D is the center of a crossing of at least three straight lines, which in the following will be called a *cobweb* structure. In this case the cobweb is located in the chaotic band at the right edge of regime D. This chaotic band ends with the transition to the period five behavior in regime E. The following regime F is again chaotic, and is bounded by the larger period-three regime G. In regimes A–G we observe a number of continuous and almost straight

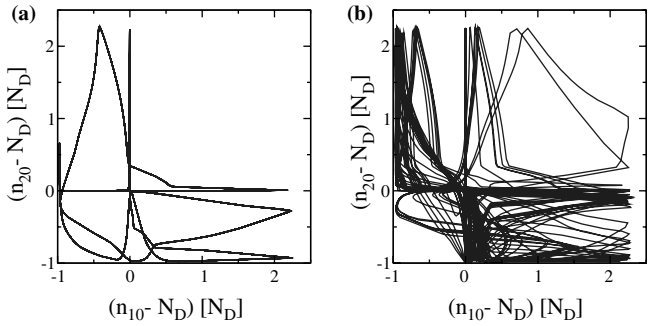

Fig. 18. Phase portrait of the electron densities n_{20} vs. n_{10} for superlattice parameters as in Fig. 1 for time series from $t = 50 \ldots 200\,\mathrm{ns}$. (a) periodic behavior at $U = 0.82\,\mathrm{V}$ and (b) chaotic behavior at $U = 1.15\,\mathrm{V}$.

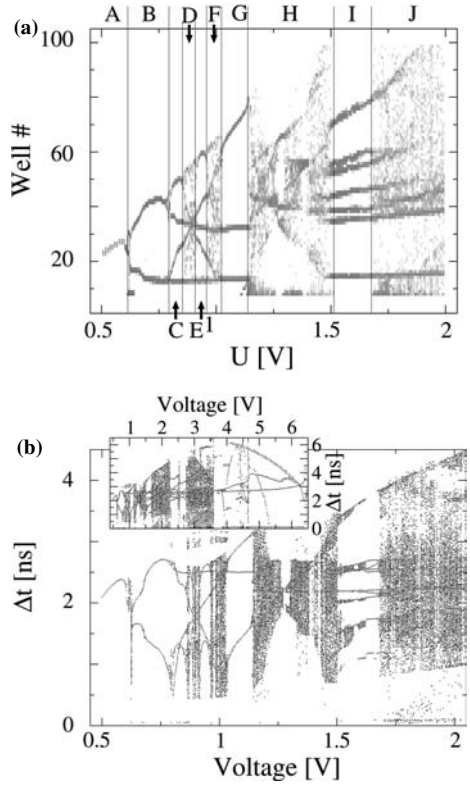

Fig. 19. (a) Positions where accumulation and depletion fronts annihilate vs. voltage at $\sigma = 0.5\ \ \Omega^{-1}\mathrm{m}^{-1}$. (b) Time differences between consecutive maxima of the electron density in well no. 20 ($n_{20}(t)$) vs voltage at $\sigma = 0.5\,\Omega^{-1}\mathrm{m}^{-1}$. Time series of length 600 ns have been used for each value of the voltage. The inset in (b) shows the time differences for a larger voltage range.

lines, which exist across various regimes, even in the chaotic regimes. These lines also give rise to the cobweb structure with its center in regime D.

In the following voltage interval H in Fig. 19, we observe collisions close to the emitter. They are the footprints of the annihilation of excitonic fronts, as discussed before. Note, however, that the numerical method for collision detection only works reliably for well numbers $m > 5$, which may limit our ability to detect excitonic collisions which occur very close to the emitter. In regime I fronts occasionally reach the collector, and we observe dynamics with seven distinct collision points. The excitonic collisions are suppressed in this regime, but they reappear in regime J, where we have fronts reaching the collector and excitonic collisions.

In principle, the position of collision p_c is a real number, but in practice it is difficult to determine p_c with an error which is less than the width of the accumulation front (cf. Fig. 14). To distinguish between chaotic and periodic behavior, we may therefore consider a suitable Poincaré section of one of the continuous dynamical system variables. This is shown in Fig. 19(b) for the time difference between two consecutive maxima of the electron density in well 20, $n_{20}(t)$. This bifurcation shows the chaotic bands at the same locations as in Fig. 19(a). We observe that chaotic and periodic behavior alternate up to a voltage of about $U = 3.6\,\mathrm{V}$, which corresponds to the case where about half of the superlattice is in the high field regime. For $U > 3.6\,\mathrm{V}$, the chaoticity suddenly disappears. From Fig. 20 we see that the reason for this change is associated with

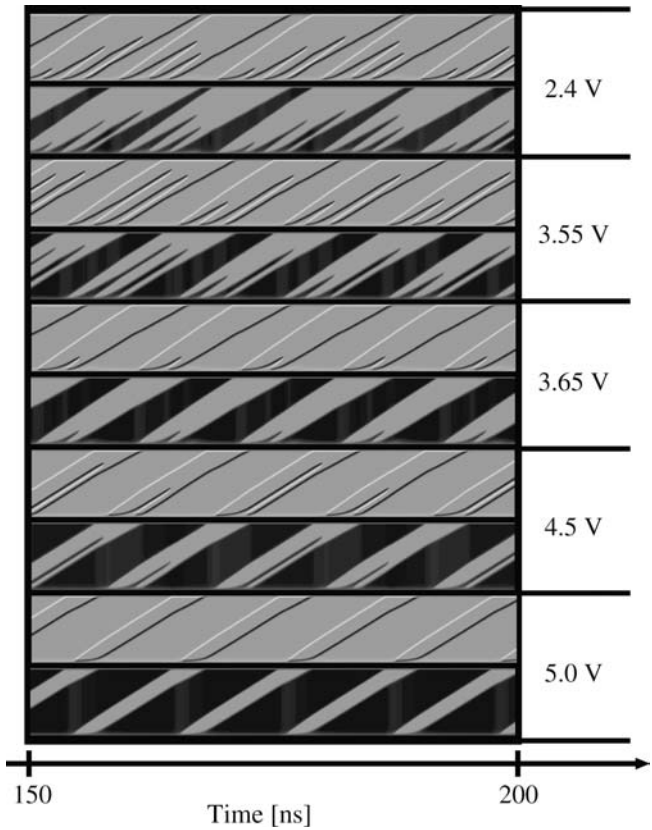

Fig. 20. Dynamic evolution of the charge densities (upper panels) and electric fields (lower panels) for various voltages. Parameters are as in Fig. 1, gray scale code as in Fig. 3.

the transition from an operation mode, in which every third high field tongue reaches the collector ($U = 3.55\,\mathrm{V}$ in Fig. 20) to a mode where only every second high field tongue reaches the collector ($U = 3.65\,\mathrm{V}$). For even higher voltages, no collisions occur, and all fronts reach the collector (cf. $U = 5.0\,\mathrm{V}$).

To further confirm the chaoticity, the largest Lyapunov exponent λ for $U \approx 1.15\,\mathrm{V}$, $\sigma \approx 0.5\,\Omega^{-1}\mathrm{m}^{-1}$) (Fig. 17) was calculated for a long ($t = 0 \ldots 100\,\mu\mathrm{s}$) time series of $n_{20}(t)$[25] using the Wolf algorithm.[55] The result $\lambda = 1.1 \times 10^9\,\mathrm{s}^{-1}$ is a clear indication of chaos.

3.1.2. Varying σ

Now that we have an idea of the bifurcations appearing for $\sigma = 0.5\,(\Omega\mathrm{m})^{-1}$, we proceed to the case of general contact conductivity. As we have learned in Section 2.3.3, the parameter σ governs the injection of fronts at the emitter. From the analysis of the case $\sigma = 0.5\,(\Omega\mathrm{m})^{-1}$ we see that the excitonic regimes (regimes H and J in Fig. 19(a)) complicate the analysis, and it would be nice if we could avoid them. This is addressed by choosing a slightly lower contact conductivity $\sigma = 0.45\,(\Omega\mathrm{m})^{-1}$, which leads to a lower critical current density, such that the condition $|j_{(1,2)}| < |j_c(\sigma)| < |j_{(2,3)}|$ holds. Furthermore, since the simplified models we will propose below are most successful in the regimes where no fronts reach the collector, we may also choose a longer superlattice. In Fig. 21 the bifurcation diagram for a superlattice with $\sigma = 0.45\,(\Omega\mathrm{m})^{-1}$ and $N = 200$ wells is shown. We see that the regimes A to G show the same behavior as the corresponding regimes in Fig. 19(a). However, the excitonic regimes have disappeared, and instead we observe a period 6 regime in regime H. Regime I shows chaotic behavior, except for a small period 7 band at its center. Furthermore we find a second cobweb structure in regime I, which shares its horizontal line with the first cobweb in regime D. The next regime J has period 5. This is followed by a small chaotic regime K, before the fronts start to reach the collector in regime L. Note how again straight continuous lines run through the whole bifurcation diagram, and are then inflected as they reach the K regime. The origins of the rich bifurcation scenario apparent in Fig. 21, including the chaotic bands, the cobweb structures and the sequence of the various periods will be explained by analytical considerations in Section 4.

We have seen that a small variation in σ has already a nontrivial effect on the bifurcation diagrams (Fig. 19 vs. Fig. 21). We may now ask, how the bifurcation diagram changes, as we further vary the contact conductivity. Since the calculation of the bifurcation diagrams is time consuming, we again use the short superlattice, with $N = 100$ wells. An

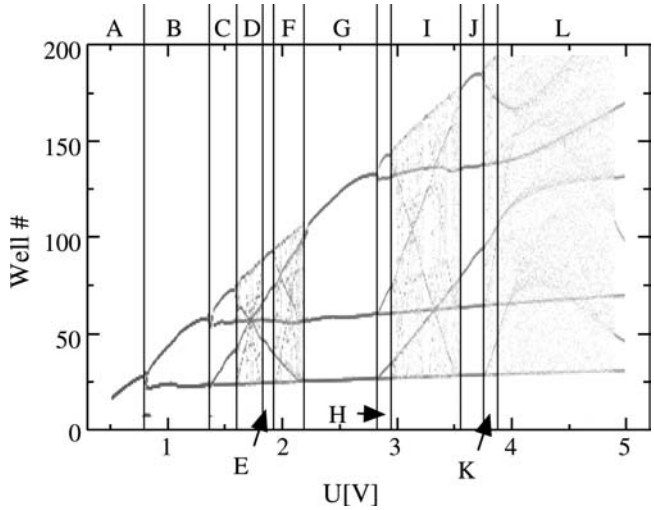

Fig. 21. Bifurcation diagram as in Fig. 19(a), but now with $N = 200$ and $\sigma = 0.45\,\Omega^{-1}\mathrm{m}^{-1}$.[56]

overview of the different bifurcation scenarios for varying σ is given in Fig. 22. We note that for $\sigma = 0.4\,(\Omega\mathrm{m})^{-1}$ the scenario resembles the situation in regimes A and B of Fig. 19, which corresponds to the periodic tripole configurations as in the first two panels of Fig. 1. We find the well known cobweb structure for $\sigma = 0.45, \ldots, 0.52\,(\Omega\mathrm{m})^{-1}$, which, however, shifts to lower voltages and lower well numbers as σ increases. For $\sigma = 0.54\,(\Omega\mathrm{m})^{-1}$, the scenario seems to have fundamentally changed. The cobweb has disappeared and the collisions close to the emitter indicate the presence of excitonic fronts. Also the familiar period-three window has disappeared, and instead we find a large period-four window, with three collision points in the sample, and every fourth front reaching the collector. A small increase to $\sigma = 0.55\,(\Omega\mathrm{m})^{-1}$ again changes the bifurcation diagram completely. Fronts reach the collector already at voltages below 1 V, and at the same time front collisions take place close to the emitter. There are now only very few continuous lines present, and the whole structure appears to be washed out. This trend continues for $\sigma = 0.57\,(\Omega\mathrm{m})^{-1}$. The bifurcation diagram for $\sigma = 0.60\,(\Omega\mathrm{m})^{-1}$ is missing in Fig. 22. The reason is that in this case no collisions within the sample occur. We have $j_c \approx j_d$, which means that we are at the symmetry point, where accumulation and depletion fronts have equal rights. At any time there are two fronts in the sample, which move in parallel, until the leading front reaches the collector and reappears at the emitter.

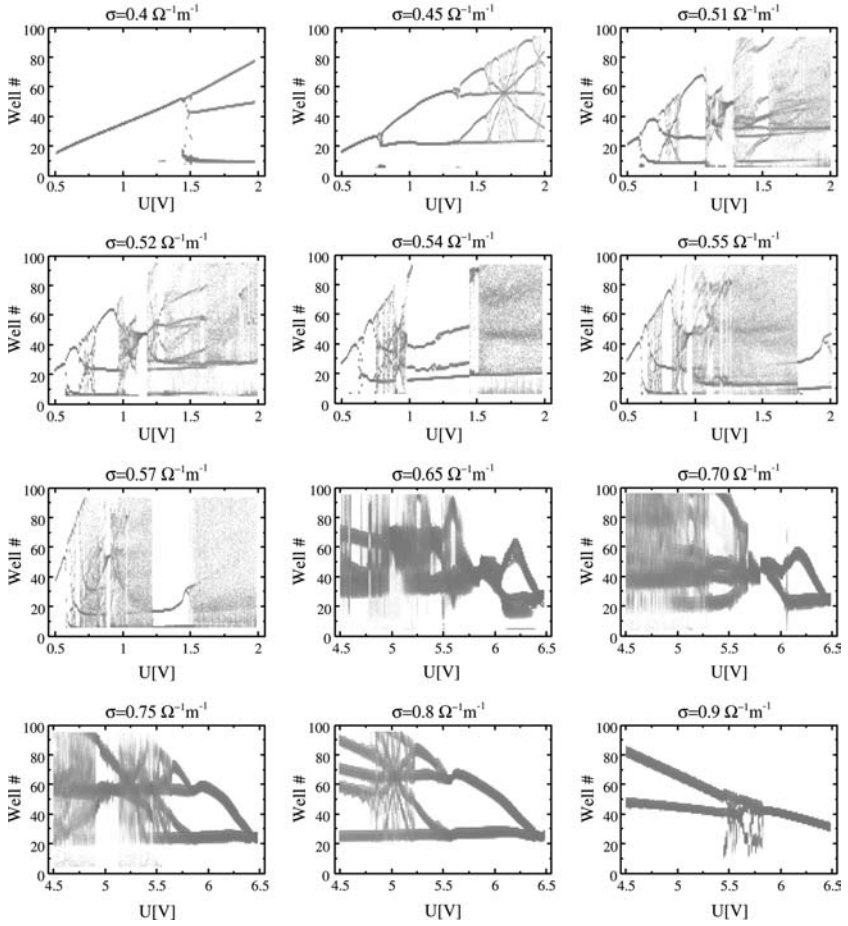

Fig. 22. Bifurcation diagrams as in Fig. 19(a), for various values of σ.

By further increasing σ, we enter the regime, where the depletion fronts are faster than the accumulation fronts. In this case it is numerically more difficult to detect the position of the annihilation with high accuracy. Thus the lines in Fig. 22 for $\sigma \geqslant 0.65\,(\Omega\mathrm{m})^{-1}$ are in general broader than before. Nevertheless the cobweb structure at $\sigma = 0.8\,(\Omega\mathrm{m})^{-1}$ is clearly visible, and also somewhat weaker for $\sigma = 0.75\,(\Omega\mathrm{m})^{-1}$. These cobwebs resemble the cobweb found at $\sigma = 0.45\,(\Omega\mathrm{m})^{-1}$ (Fig. 21), but is flipped along the voltage axis. This is a consequence of the symmetry transformation, which we discuss below. Another interesting feature is the reconnection of the period doubling bifurcation, which occurs at $\sigma = 0.7\,(\Omega\mathrm{m})^{-1}$ and

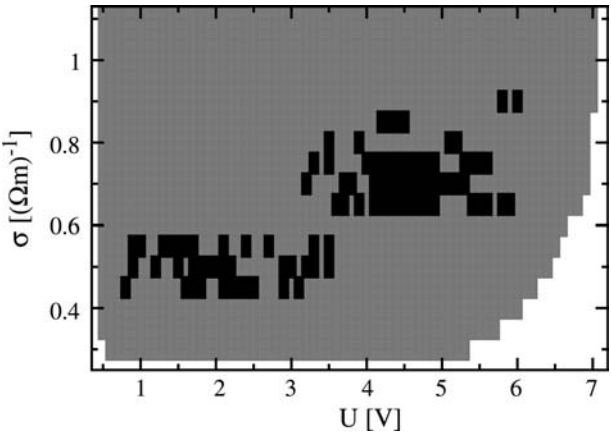

Fig. 23. Two parameter bifurcation diagram. Black squares: chaotic behavior; gray shading: periodic oscillations; white region: absence of oscillations.[25]

$\sigma = 0.65\,(\Omega\mathrm{m})^{-1}$, and causes a distinct bubble like structure in the bifurcation diagram.

It is now interesting to plot a "phase-diagram" of chaotic behavior in the (U, σ)-plane as shown in Fig. 23, which was obtained by considering the autocorrelation function $C(\tau) = \langle n_{20}(t) n_{20}(t+\tau)\rangle_t$.[25] For periodic behavior $C(\tau)$ does not decay even for large values of $\tau > 20$ ns, while for chaotic behavior $C(\tau)$ decays with a correlation time less than 20 ns. We note that chaotic behavior is only possible, if we choose σ such that $|j_{(1,2)}| < |j_c(\sigma)| < |j_{(2,1)}|$. Furthermore there exist two larger disjoint regions whose gross features are reminiscent of an inversion symmetry about a point at $(U \approx 3.5\,\mathrm{V}, \sigma \approx 0.6\,\Omega^{-1}\mathrm{m}^{-1})$. The origin of this "symmetry" is the approximate invariance of the system under the simultaneous permutation of accumulation with depletion fronts, and low-field with high-field domains.

3.2. The Front Model

We are now in a position to approximate the microscopic dynamics of the electron densities n_i by means of a simple front model, in which the positions of the accumulation fronts $a_1 \ldots a_{N_a}$ and the depletion fronts $d_1 \ldots d_{N_d}$ and the overall current j are the new dynamical variables. Here N_a and N_d denote the number of accumulation and depletion fronts in the system. We will see that this step from the microscopic description to a front description does not only greatly reduce the dimensionality of the

system, but also the number of physical parameters. The introduction of front positions was already shown to be useful in Section 2.2 for the case of the free motion of noninteracting fronts far away from the boundaries. We now make the assumption that the essential dynamics of the system can be described in terms of front positions, even if the fronts are close to each other or close to the boundaries. Such a "dilute gas" approximation will obviously fail if the density of fronts is large or if the typical time scale for interactions between fronts can not be assumed to be small.

3.2.1. The Rules for the Front Model

Let us write (28) as

$$\frac{v_d(j)}{v_a(j)} = \frac{N_a}{N_d}. \tag{37}$$

By formally inverting the left hand side of (37) and taking into account the results of Section 2.2 we arrive at

$$j = j_{(N_a,N_d)} = j\left(\frac{N_a}{N_d}\right), \tag{38}$$

which is a monotonically increasing function, since v_d (v_a) is monotonically increasing (decreasing). We can therefore replace the condition $|j| < |j_c|$ appearing in rule GI′ (Sect. 2.3.3) by an equivalent condition

$$\frac{N_a}{N_d} < r_c, \tag{39}$$

where the parameter r_c is defined by $j_c = j(r_c)$. A similar statement applies to rule GII′. We have therefore managed to enslave the current density j to the fraction N_a/N_d. Note that in particular $j_d = j(1)$.

For the analysis of the bifurcation scenario, it is sufficient to consider the dynamics in the Poincaré section which is defined by the hyperplane, where N_a or N_d change. The absolute time between such events is not important, and we are therefore free to rescale the velocities to our convenience. In the following we rescale time such that $v_a + v_d = 2$, which together with (37) gives the front velocities as

$$v_a = \frac{2N_d}{N_a + N_d}, \qquad v_d = \frac{2N_a}{N_a + N_d}. \tag{40}$$

We require that the fronts evolve according to (40), until an event which changes the number of fronts occurs. Such an event may be the generation of a new front at the emitter according to the rules GI′ and GII′ as described in Section 2.3.3. Furthermore two fronts can collide as described in Section 2.3.1, which will simply eliminate the corresponding d_i and a_i from the system of variables and decrease N_a and N_d accordingly by one. The third possibility is the annihilation of a front at the collector as described in (Section 2.3.2). We may summarize the complete front model by the following set of rules:

FI The positions of the accumulation fronts a_i for $i = 1 \dots N_a$ and depletion fronts d_i for $i = 1 \dots N_d$ evolve according to $\dot{a}_i = v_a$ and $\dot{d}_i = v_d$ with the velocities (40) until one of the following rules applies.

FII If $N_a/N_d < r_c$ and $p_h < d_1 < a_1$ then increase N_a by one, re-index $a_i \to a_{i+1}$ for all i and set $a_1 = 0$ (injection of accumulation front).

FIII If $N_a/N_d > r_c$ and $p_l < a_1 < d_1$ then increase N_d by one, re-index $d_i \to d_{i+1}$ for all i and set $d_1 = 0$ (injection of depletion front).

FIV If $a_{i'} = d_{j'}$ for any i', j' then decrease N_a and N_d by one, re-index $a_{i+1} \to a_i$ for $i \geqslant i'$ and $d_{j+1} \to d_j$ for $j \geqslant j'$ (annihilation of front pair).

FV If $a_{N_a} > L$ decrease N_a by one (accumulation front hits collector).

FVI If $d_{N_d} > L$ decrease N_d by one (depletion front hits collector).

Here p_h and p_l are the phenomenological distance parameters from GI′ and GII′ (Section 2.3.3), which suppress the front generation for $d_1 \leqslant p_h$ and $a_1 \leqslant p_l$, respectively.[57]

The only parameters appearing in the front model are r_c, p_h and p_l, which govern the generation of new fronts at the emitter and L, which influences the annihilation at the collector. The voltage parameter L_h is connected to the voltage by (23), and in principle also depends weakly on N_a/N_d due to (38), but for simplicity we consider L_h to be constant, which is a good approximation, if

$$\left| \frac{\partial L_h}{\partial j} \frac{j_{(1,2)} - j_d}{L_h} \right| \approx \left| \frac{\partial F_h}{\partial j} \frac{j_{(2,1)} - j_d}{F_h} \right| \ll 1. \tag{41}$$

Then L_h only enters in the initial condition for the front positions (see Eq. (24)). These five parameters should be contrasted to the large set of parameters of the microscopic model.[22] However, in particular p_h and p_l might be difficult to derive quantitatively from the microscopic model, and should rather be regarded as *fit parameters*. Again p_h and p_l can in

principle depend on N_a and N_d, but for simplicity we assume them to be constant.

The dynamical variables of the systems are the positions d_i and a_i of the fronts. Due to the constraint given by (24), the number of degrees of freedom is then given by $f^d = N_a + N_d - 1$. Let us define $N_{a/d}^{\max}$ as the maximum possible values of $N_{a/d}$, respectively, and define the parameter n as

$$n = \max\left[N_a^{\max}, N_d^{\max}\right]. \tag{42}$$

Then we have $f^d \leqslant N_a^{\max} + N_d^{\max} - 1 = 2n - 2$, which in general is much smaller than N, the number of degrees of freedom of the full microscopic model. It is however a peculiarity of this system that f^d changes dynamically. To avoid the mathematical complications that arise from the fact that the number of dynamical system variables is not constant, we formally extend the arrays of front positions to the maximal possible size, $a_1, \ldots, a_{N_a^{\max}}$ and $d_1, \ldots, d_{N_d^{\max}}$ and consider additionally N_a and N_d as discrete system variables. The new additional front positions $a_{N_a+1} \ldots a_{N_a^{\max}}$ and $d_{N_d+1} \ldots d_{N_d^{\max}}$ do not appear in the front rules FI–FVI and we can just set them to zero for definiteness. By this formal transformation we have now obtained a system with $N_a^{\max} + N_d^{\max}$ continuous and two discrete variables.[5] This type of system therefore belongs to the mathematical class of *hybrid* systems. Hybrid models are of fundamental interest in the field of theoretical computer science, where they are used to describe the interaction of a digital (i.e. discrete) computer with an analog environment.[58]

Note that the rules of the front model are invariant under the simultaneous transformation of

$$\begin{gathered} a_i \leftrightarrow d_i, \qquad N_a \leftrightarrow N_d, \qquad p_h \leftrightarrow p_l, \\ r_c \to \frac{1}{r_c}, \qquad L_h \to L - L_h, \end{gathered} \tag{43}$$

i.e. accumulation and depletion fronts are exchanged, r_c is inverted, and the high field and low field domains are exchanged ($L_h \to L - L_h$). This exact symmetry can therefore explain the qualitative point symmetry found in Fig. 23, since the transition $r_c \to r_c^{-1}$ induces a corresponding transformation $\sigma(j(r_c)) \to f^s(\sigma(j(r_c)))$ with the fixed point $\sigma(j_d) = f^s(\sigma(j_d))$.

[5]Since the product of two countable sets is also countable, we may as well replace the two discrete variables by only one.

In view of the symmetry of (43) we may restrict our analysis to the case $r_c < 1$. We will see in Section 4 that in this case the length of the high field domains can be easily identified with the filling heights in a tank model. Note, however, that in device physics the case $r_c > 1$ is often considered to be more realistic since it corresponds to a large emitter conductivity.[20,38]

We furthermore set $p_l = 0$ since the accumulation fronts are rather narrow and should not suppress the generation of a trailing depletion front. In this case rule FIII always applies, if the first front is an accumulation front, since in this case $N_a/N_d \geqslant 1$ and injects a new depletion front. On the other hand rule FII can only apply if $N_d = N_a + 1$. It does not apply as long as $N_a > r_c/(1-r_c)$ and N_a can then only decrease, since FII is the only process which generates new accumulation fronts. Consequently r_c imposes the following limits on the number of fronts:

$$N_d < \frac{1}{1-r_c} + 1, \quad N_a < \frac{1}{1-r_c}. \tag{44}$$

By comparing with (42) we find that for $r_c < 1$, the parameter n is the largest integer less than $1/(1-r_c)+1$. The dependence of the maximum front numbers $N_a^{\max}$ and $N_d^{\max}$ on r_c is summarized in Table I.

Once the conditions for FII are fulfilled and an accumulation front is injected, it is immediately followed by the injection of a depletion front due to rule FIII. Effectively we therefore inject a pair of fronts, i.e. a

Table I. Maximum Possible Number of Accumulation and Depletion Fronts and the Number of Necessary Tanks n (see Section 4.2) for Various Values of r_c

r_c	n	$N_a^{\max}$	$N_d^{\max}$
0	1	0	1
$(0, \frac{1}{2}]$	2	1	2
$(\frac{1}{2}, \frac{2}{3}]$	3	2	3
$(\frac{2}{3}, \frac{3}{4}]$	4	3	4
$(\frac{n-2}{n-1}, \frac{n-1}{n}]$	n	$n-1$	n
1	∞	∞	∞
$[\frac{n}{n-1}, \frac{n-1}{n-2})$	n	n	$n-1$
$[\frac{3}{2}, 2)$	3	3	2
$[2, \infty)$	2	2	1
∞	1	1	0

dipole, with a leading accumulation and a trailing depletion front. In the language of field domains, this process detaches a high field domain from the emitter and opens a new one.

In Table I we also list the parameter n for various values of r_c. Since n is invariant under the symmetry transformation (43), we propose that n will be a suitable parameter for classifying different bifurcation behavior. Indeed we will see in Section 4 that n corresponds to the number of tanks which are necessary to describe a given dynamics.

3.2.2. The Case $n = 3$

The numerical integration of the front model is facilitated by the fact that the evolution of the front positions is piecewise linear due to FI with the velocities given in (40). We can therefore calculate the times $t_{\mathrm{FII}}, \ldots, t_{\mathrm{FVI}}$, until the corresponding conditions in FII ... FIV would be fulfilled under the assumption that N_a and N_d would not change. The actual event is then determined by the minimum time t_{FX}, with X = II ... VI. The fronts are then moved to the new positions $a_i' = a_i + t_{\mathrm{FX}} v_a$ and $d_i' = d_i + t_{\mathrm{FX}} v_d$, and the changes in the discrete variables N_a and N_d are performed as prescribed by the respective rule FX.

The numerical solution of the front model for $p_l = 0$, and $N_a^{\max} = 2$ yields a typical front pattern as in Fig. 24. We see that for small L_h the front which is closest to the collector, is always a depletion front. Since the fronts are generated in pairs at the emitter, we have $N_d = N_a + 1$, and therefore $v_a > v_d$. That means that the accumulation fronts can catch up and annihilate with preceding depletion fronts. This is the same behavior as observed in Section 2.3.1 for the microscopic model. In fact the front pattern at low L_h in Fig. 24 can be directly related to the ones in Fig. 1. As a particular striking example compare the period seven orbits at $L_h = 0.202$ in Fig. 24 and at $U = 0.98\,\mathrm{V}$ in Fig. 1. As long as the fronts do not reach the collector, the only relevant length scale for L_h is the distance parameter p_h. In the microscopic model, this parameter corresponds to the minimal distance between the first depletion front and the newly generated accumulation front and will in general depend on the buildup time of the accumulation front and other microscopic parameters in a complicated way.

In its present form the front model is not chaotic, which is in contrast to the full microscopic model. Instead arbitrarily long stable periodic orbits are possible. We will discuss Section 4, how chaoticity can be introduced in a generic way. At higher values of L_h, we find the characteristic "tongues" ($L_h = 0.595$ in Fig. 24), which also occur in the microscopic model (see $U = 3.55\,\mathrm{V}$ in Fig. 20), but we did not succeed in finding

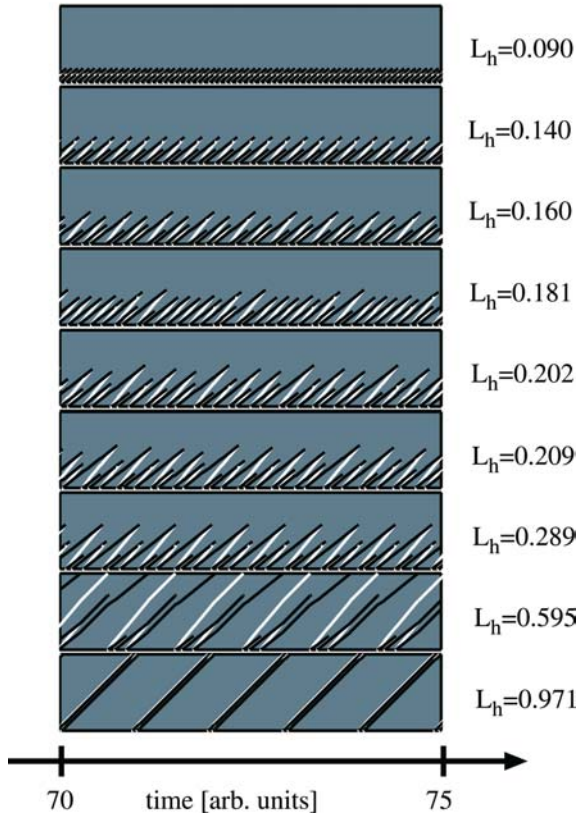

Fig. 24. Front evolution in front model for $n=3$, $p_l=0$, $p_h=0.115$, $r_c=0.51$, $L=1$ and various values of L_h. Accumulation (depletion) fronts are denoted by white (black) lines. L_h corresponds to the voltage U in the microscopic model (cf. Figs. 1 and 20).

the other patterns in Fig. 20. One reason, why the front model does not describe well the high L_h case becomes apparent, if we compare $L_h=0.971$ in Fig. 24 and $U=4.5\,\mathrm{V}$ in Fig. 20, where fronts of opposite polarity traverse the whole superlattice at only a very small distance to each other. This is obviously not possible in the microscopic approach, since the fronts would tend to annihilate. Thus the front model can still be improved in the high voltage regime.

A further touchstone for the usefulness of the front model is given by its bifurcation diagram as shown in Fig. 25. The prominent feature is again the cobweb-like pattern at low voltages, which has a striking similarity with the corresponding patterns in Fig. 19(a) and Fig. 21. In fact

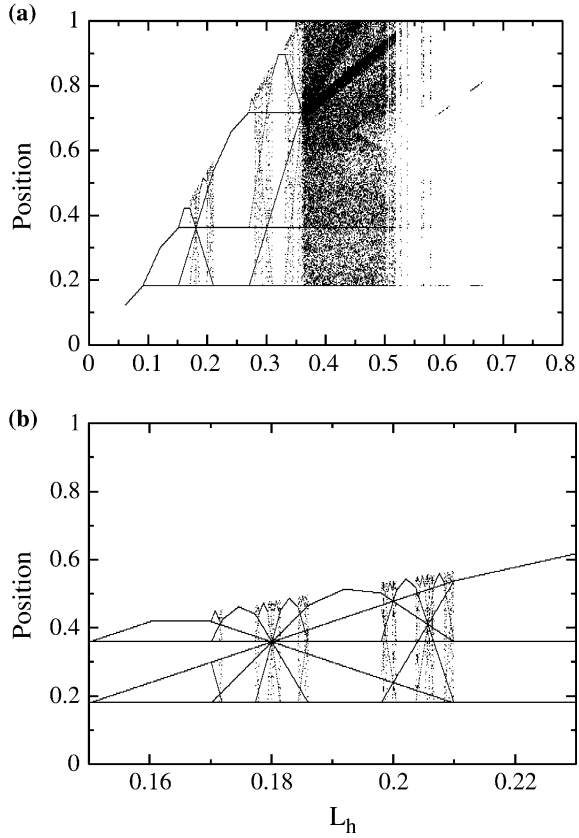

Fig. 25. Bifurcation diagrams for positions of front collision vs L_h obtained from the front model for $n=3$ on two different scales of L_h. Parameters: $p_h=0.06$, $p_l=0$, $r_c=0.52$, $L=1.0$.

all regions from A to K of Fig. 21 can also be identified in Fig. 24, only region K does not fit perfectly. In particular, the vertical bands in Fig. 25(b) can be identified with the three chaotic bands in the regions D and F of Fig. 21. However, since the front model is not really chaotic in this regime, they actually consist of ever finer subbands as shown in the lower panel of Fig. 25. Apparently a period of more than seven different collision points appears chaotic in the microscopic model. Another feature of the original bifurcation scenario that is well reproduced by the front model is that the chaotic behavior suddenly becomes periodic at about $L_h=0.53$. On the other hand, we do not observe periodic windows for $L_h \in [0.36, 0.53]$ which were present in the microscopic model.

The fact that the topology of the nontrivial pattern up to the large period three window $U=1.1\,\mathrm{V}$ in Fig. 19 can be reproduced by the simple

rules of the front model is a hint that such a pattern might be even more generic, as we will see in Section 4.

We could now proceed to extract the detailed features of the bifurcation diagram by a thorough analysis of the algebraic properties of the front model. For example the horizontal lower line appearing in Fig. 25 is caused by p_h. If $N_a = 1$ and $N_d = 2$, we can inject a new accumulation front by FII as soon as d_1 has reached p_h. As argued before, this will entail as well the injection of a depletion front, and we have the situation:

$$N_a = 2, \quad N_d = 3, \quad a_1 = d_1 = 0, \quad d_2 = p_h, \quad d_3 - a_2 = L_h - p_h. \tag{45}$$

From (40) we get $v_a - v_d = 2/5$. If now additionally $L_h > 2p_h$, it follows that $d_3 - a_2 > d_2 - a_1$ and therefore the fronts d_2 and a_1 will be the first to annihilate. If $L_h > 3/2p_h$, then the fronts d_3 and a_2 will be the first to annihilate, but by that time $d_1 > p_h$ and therefore a new dipole is immediately injected at the emitter. This maintains the velocities of the original d_2 and a_1 and in both cases the collision occurs at a position

$$p^{z1} = p_h \frac{v_a}{v_a - v_d} = np_h. \tag{46}$$

For $n = 3$ and $p_h = 0.06$ this yields the horizontal line in Fig. 25 at $p^{z1} = 0.18$. A further analysis of the structure of the bifurcation diagram along these lines is possible, but cumbersome. We will therefore in the next section introduce a model which is better suited to an analytical approach.

3.2.3. Arbitrary n

In Fig. 26 the bifurcation diagrams of the front model for $n = 4$ and $n = 5$ are plotted. After the successful identification of many common features in the bifurcation diagrams of the microscopic model and the front model for $n = 3$, we would hope that at least some features from Fig. 26 also appear in one of the panels of Fig. 22. However, this is apparently not the case. The reason for this failure seems to be that with a large number of fronts, the approximation that fronts can be considered as independent point-like "quasi-particles" breaks down. In the language of statistical physics, the dilute gas approximation is no longer valid, and we have to take into account three front interactions, and other complications. We may speculate, however, that for very large superlattices with narrow fronts, a bifurcation scenario as in Fig. 26 should arise.

It is nevertheless still interesting to scan the (L_h, r_c) plane of the front model for regions of long periods, since they correspond to chaotic

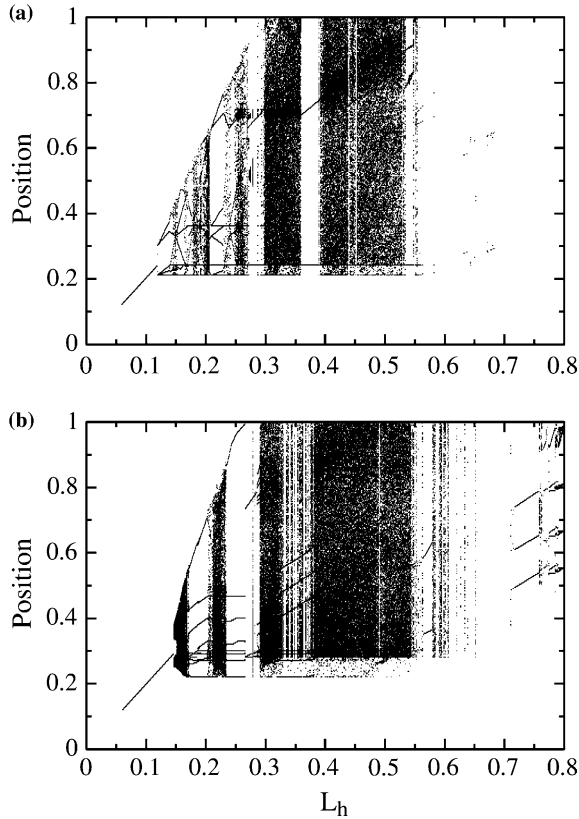

Fig. 26. Bifurcation diagrams for positions of front collision vs L_h obtained from the front model for (a) $n=4$ ($r_c=0.67$) and (b) $n=5$ ($r_c=0.76$). Parameters: $p_h=0.06$, $p_l=0$, $L=1.0$.

regimes of the microscopic model. By varying r_c and L_h simultaneously we obtain the two parameter bifurcation diagram of Fig. 27. Note that the broad horizontal bands in Fig. 27 are due to the fact that the changes in r_c within the intervals given by Table I do not affect the dynamics of the system. The basic structure of the bifurcation diagram obeys the symmetry of (43) and conforms well with the corresponding bifurcation diagram of the microscopic model in Fig. 23.

4. THE TANK MODEL

In the previous section we have introduced a simple front model, which astonishingly well reproduces many features of the complex microscopic model, at least in the low and intermediate voltage regimes, when

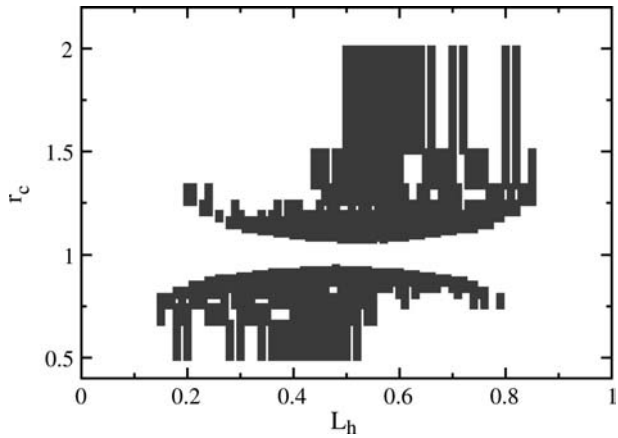

Fig. 27. Two parameter bifurcation diagram for the front model. Dark region corresponds to (L_h, r_c) pairs with at least 10 different points of front collisions. Parameters: $L = 1.0$; for $r_c < 1$: $p_h = 0.06$, $p_l = 0$; for $r_c > 1$: $p_h = 0$, $p_l = 0.06$. In the microscopic superlattice model, L_h and r_c correspond to U and σ, respectively (cf. Fig. 23).

no fronts reach the collector. We will now further simplify the front model in this regime and will finally arrive at a *tank model*. Such models have been extensively studied in computer science and applied mathematics, since they describe the dynamic of production processes.[30,59] Typically one obtains a "strange billiard" behavior,[60,61] which means that the system evolves piecewise linearly, and only changes its direction at the boundary of a specific domain. The advantage of such an approach is that these type of models can often be treated analytically. As we will see, this simplification allows us to relate the bifurcation scenario of the front system to the bifurcations obtained in a simple low dimensional iterated map. In the most simple nontrivial case this map will be only one-dimensional.

A connection between maps and single fronts has previously been studied in the case of coupled map lattices[62] and for periodically driven systems.[63] In contrast to those works, however, we are here concerned with the use of maps for a system with interacting fronts.[57]

4.1. Derivation from the Front Model

Let us now derive the tank model from the front model in Section 3.2. The idea is that instead of dealing with the position of accumulation and depletion fronts, we restrict ourselves to the dynamics of the high field domains, which appear between two fronts, or between the emitter and the first depletion front. Technically it is again easier to start with

the case $p_l = 0$, but we will see that in principle, the tank model even holds for general p_l.

4.1.1. The Case $p_l = 0$

We again assume $r_c < 1$ and for the moment $p_l = 0$. Our first task is to derive a condition, for which no fronts will reach the collector. We consider a situation where $N_d = N_a + 1 \leqslant n$, at the point in time where a dipole is injected at the emitter by the rules FII and FIII of the front model (see Section 3.2). We then have $a_1 = 0$, $d_1 = 0$ and $d_2 \leqslant L_h$ by (24). From (40) we see that $v_a - v_d \geqslant 2/(2n-1)$ and therefore the time until a_1 and d_2 collide will be $t^{\text{collision}} \leqslant L_h(n - 1/2)$. On the other hand we have $v_a < 4/3$ and therefore the time until a_1 reaches the collector is $t_a^{\text{transit}} > 3L/4$. We may then conclude that no fronts reach the collector if $t^{\text{collision}} < t_a^{\text{transit}}$, or equivalently

$$L_h \left(n - \frac{1}{2} \right) < \frac{3}{4} L. \tag{47}$$

For $n = 3$ and $p_l = 0$, (47) states that for $L_h < 0.3L$ no fronts will reach the collector, which is confirmed by our simulation of the front model (Fig. 25). From now on we assume that (47) is fulfilled.

The essential step in the derivation of the *tank model* is that we now choose the lengths of the high-field domains,

$$x_1 = d_1, \tag{48}$$

$$x_i = d_i - a_{i-1} \quad \text{for } i = 2 \ldots N_d, \tag{49}$$

as the new dynamical variables of the system (cf. Fig. 28). Here x_1 is special, since it is the high-field domain, which is connected to the emitter, and is therefore only bounded by a depletion front. This is in contrast to all other high field domains which are bounded by a depletion front from above and an accumulation front from below. The introduction of the new variable x_i reduces the number of continuous system variables from $2n-1$ to n. We hereby lose the information on the position of the high field domain within the superlattice. But the absolute front positions do only occur in the rules FV and FVI of the front model, and they will not apply, since we assumed that no domains will reach the collector. If $p_l = 0$, the condition $N_a = N_d - 1$ is always fulfilled and we need to keep track of only one discrete variable N_d. The global constraint (24) is translated to the new variables by

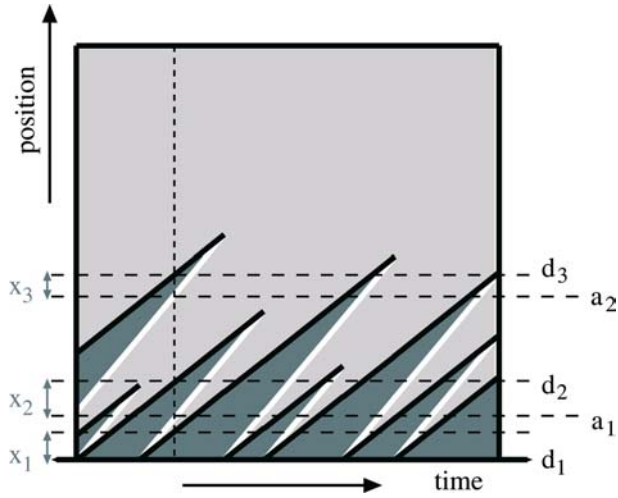

Fig. 28. High-field domain variables x_i derived from front positions a_i (white lines) and d_i (black lines). The dark shaded areas denote the high field domains.

$$L_h = \sum_{i=1}^{N_d} x_i. \tag{50}$$

From the front velocities (40) we may obtain the shrinking and growing velocities of the high-field domains by

$$\dot{x_i} = \begin{cases} v_d = \frac{2N_d-2}{2N_d-1} & \text{if } i=1, \\ v_d - v_a = -\frac{2}{2N_d-1} & \text{else.} \end{cases} \tag{51}$$

$$= -\mu + \lambda\delta_{i1}, \tag{52}$$

with

$$\mu = \frac{2}{2N_d-1}, \qquad \lambda = N_d\mu. \tag{53}$$

The conditions for rule FII are expressed in terms of the new variables, by requiring that $N_d < n$ and $x_1 < p_h$. As usual FIII follows FII, and this combination detaches a high field domain from the emitter and creates a new one. The conditions for the collision rule FIV is rephrased by requiring that one of the x_i becomes zero.

We can then summarize this model by the following set of rules:

TI The high-field lengths x_i evolve according to (51) until one of the following rules applies.

TII If $N_d < n$ and $x_1 > p_h$ then increase N_d by one, re-index $x_i \to x_{i+1}$ for all i and set $x_1 = 0$.

TIII If $x_{i'} = 0$ then decrease N_d by one, re-index $x_{i+1} \to x_i$ for all $i \geqslant i'$.

In the following we will refer to the rules TI–TIII together with the initial condition (50) as the *tank model*. The reason for this name will become obvious in Section 4.2. The tank model has n continuous dynamical variables $x_i, i = 1 \ldots n$ and one discrete dynamical variable N_d. Like the front model (see Section 3.2) it is therefore a *hybrid* model. It furthermore depends on one discrete parameter n, and the two continuous parameters p_h and L_h.

4.1.2. The Case $p_l > 0$

The above derivation of the tank model was restricted to the special case $p_l = 0$. This restriction is not necessary for the derivation of the tank model, and we now show that for general p_l the rules TI–TIII are still valid without modification, although the condition (47) and the definition of the time axis has to be adapted.

For $p_l > 0$ the front model rule FIII does not follow immediately FII, but the injection of the depletion front is delayed, until $a_1 > p_l$ is fulfilled. During this time we have $N_a = N_d$ and hence $v_a = v_d = 1$, which means that no collisions occur, and all front positions are just increased by p_l. Equivalently, instead of adding the constant p_l to every front position, one can also reduce the effective lattice length L by the amount p_l each time a new accumulation front is injected. During the transit of an accumulation front to the emitter, this may happen at most $L/(p_h + p_l) + 1$ times, since two accumulation fronts are at least separated by a distance $p_l + p_h$. Therefore the condition (47) that no fronts reach the collector has to be modified for the case $p_l \neq 0$ to read

$$L_h \left(n - \frac{1}{2} \right) < \frac{3}{4} \left(L \frac{p_h}{p_l + p_h} - p_l \right). \tag{54}$$

Furthermore during the time between FII and FIII, all high-field fronts are bounded by an accumulation and a depletion front and $\dot{x}_i = 0$ for all i. The net effect of a non vanishing p_l is then to increase the time variable by the amount p_l, each time a high-field front is disconnected from the emitter, but otherwise follow the rules TI–TIII. This effect will obviously not influence the dynamic bifurcation scenario,

and can be eliminated completely by a suitable redefinition of the time axis.

4.2. Connection to Water Tanks

Let us now justify the use of the term *tank model* for the model described by the rules TI–TIII, by showing that surprisingly the same set of rules describes a completely different system. Consider a system of n water tanks as in Fig. 29. Here a switching server fills one of the tanks with a filling rate λ, and at the same time all N_d nonempty tanks drain at a rate $-\mu$. To keep the total amount of water at a constant value L_h, we require $\lambda = \mu N_d$. The server switches to one of the $n - N_d$ empty tanks only under the condition that the tank which it is currently filling has already reached the minimum filling height p_h. This model is equivalent to what we formulated by the rules TI–TIII and the initial condition (50). The variables x_i of the high field domains are up to some trivial re-indexing the filling heights of the water tanks. The high-field domain x_1 at the emitter is interpreted as the tank connected to the server, while the other nonempty tanks represent detached high field domains inside the superlattice. A switching of the server corresponds to the detaching of the old high field domain at the emitter, and the generation of a new one by TII. The rule that the server should not switch if the currently filled tank has a filling height less than p_h, obviously agrees with the requirement of TII that a high field domain

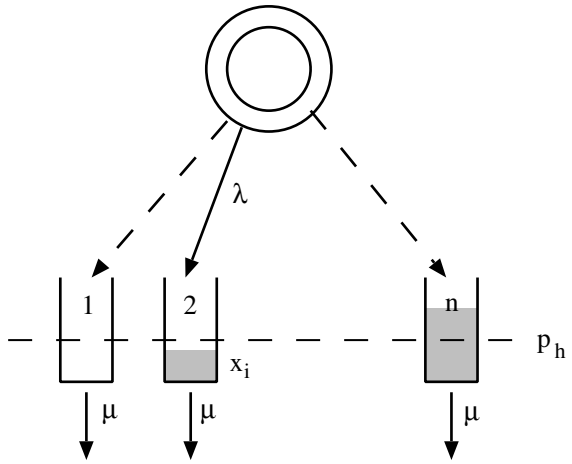

Fig. 29. Scheme of an n-tank switched arrival system with minimal filling height p_h. The server filling rate is λ, the draining rate of all tanks is $-\mu$.

may only be detached from the emitter, if it has a certain minimal length p_h. The constant amount of water corresponds to the constant total length of the high-field regime L_h.

Variants of such models are well studied in the context of production processes.[59] For example, in[61] a model with a *maximum* filling height was considered. In computer science similar models are relevant for the description of *queuing systems*,[64] where the server can, for example, represent a CPU, and the tanks are the different tasks, which should be served by the CPU. Even the requirement of a minimal filling height makes sense in this context, since in a multitasking computer system, the switching of the task involves a certain overhead, which forbids arbitrarily fast task switching.

4.3. The Poincaré Map

A natural way to proceed is to consider a suitable Poincaré section. Since all tanks with the exception of tank #1, which is connected to the server, are equivalent, we now adopt the sorting convention that $x_i > x_{i+1}$ for $i \geqslant 2$. Thus the dynamics of the system is confined to an $n-1$ dimensional simplex of the form:

$$A^n = \left\{ \mathbf{x} \in \mathbb{R}^n \,|\, \sum_{j=1}^{n-i} x_j = L_h \wedge x_1 \geqslant 0 \wedge x_2 \geqslant \cdots \geqslant x_n \geqslant 0 \right\}. \tag{55}$$

As a suitable hyperplane for the Poincaré section we consider the $n-2$ dimensional simplex

$$B^n = \{\mathbf{x} \in A^n \,|\, x_1 \geqslant p_h \wedge x_n = 0\}, \tag{56}$$

which precisely contains the set of points, for which the conditions of rule TII are fulfilled. A sketch of A^n and B^n for the case $n=3$ is shown in Fig. 30.

Let us assume that at a certain time t_m we have $\mathbf{x}(t_m) \in B^n$. We now look for a Poincaré map

$$P^n: \quad B^n \to B^n, \quad \mathbf{x}(t_m) \mapsto \mathbf{x}(t_{m+1}), \tag{57}$$

which relates $\mathbf{x}(t_m)$ to the point $\mathbf{x}(t_{m+1})$ of the next visit of the simplex B^n. For $n=2$ the simplex B^2 is reduced to a point $B^2 = \{(L_h, 0)\}$, which by P^2 is simply mapped onto itself. The dynamics is therefore trivially periodic. In the following we assume $n \geqslant 3$.

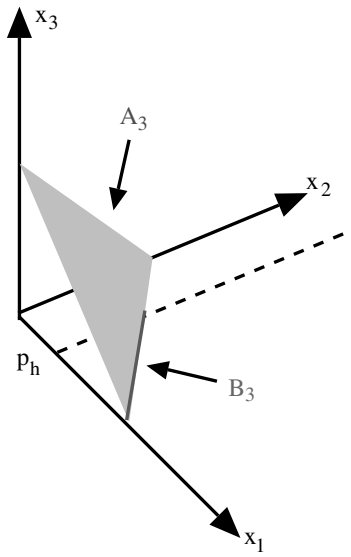

Fig. 30. Sketch of the simplex A^3 (55) and the Poincaré section B^3 (56) for $n=3$.

The application of rule TII at t_m triggers the generation of a new high field domain at the emitter, or in the language of water tanks, the switching of the server to a new tank. This is achieved by a relabeling of the tank indices such that old x_1 is enqueued among the $x_2 \dots x_{n-1}$ and the new x_1 is set to zero. Explicitly we write

$$\mathbf{x}(t_m^+) = M^{\mathrm{TII}}\mathbf{x}(t_m), \tag{58}$$

where t_m^+ denotes the time just after the application of TII. The matrix M^{TII} takes care of the ordering of the filling heights and is given by

$$M^{\mathrm{TII}} = \begin{cases} \delta_{j_0,j} & \text{for } j=1, \\ \delta_{i,j} & \text{for } 2 \leqslant j < j_0, \\ \delta_{i+1,j} & \text{for } j \geqslant j_0 \end{cases} \tag{59}$$

$$\text{with } x_{j_0-1}(t_m) \geqslant x_1(t_m) \geqslant x_{j_0}(t_m). \tag{60}$$

In particular we note that

$$x_1(t_m^+) = 0, \tag{61}$$

$$x_n(t_m^+) = \min\left(x_{n-1}(t_m), x_1(t_m)\right) \tag{62}$$

and therefore $\mathbf{x}(t_m^+) \notin B^n$. This guarantees that $t_{m+1} > t_m$.

We first consider the case with $(n-1)x_n(t_m^+) > p_h$, which by (62) is equivalent to

$$(n-1)x_{n-1}(t_m) > p_h. \tag{63}$$

Then the tank #1 receives water from the $n-1$ other tanks, and will have reached the filling height p_h before tank #n is empty. Therefore the time t_{m+1}, at which $\mathbf{x}(t)$ visits B^n is given by

$$t_{m+1} = t_m + \frac{x_n(t_m^+)}{\mu}. \tag{64}$$

For $t \in [t_m^+, t_{m+1}^-]$ there are no empty tanks, i.e $N_d(t) = n$, and we may write explicitly

$$x_i(t_{m+1}) = \begin{cases} (n-1)x_n(t_m^+) & \text{for } i = 1, \\ x_i(t_m^+) - x_n(t_m^+) & \text{for } i = 2 \ldots n-1, \\ 0 & \text{for } i = n. \end{cases} \tag{65}$$

In the case that (63) is not fulfilled, the last tank is empty before the first tank has reached its minimal switching height p_h. The switching time t_{m+1} is therefore determined by the condition $x_1(t_{m+1}) = p_h$. For the construction of the Poincaré map, we need to know the number of nonempty tanks $\tilde{N}_d$ at the time t_{m+1}^- just before we visit B^n. A little thought shows that this is given by

$$\tilde{N}_d = N_d(t_{m+1}^-) = \max \left\{ k \in \mathbb{N} \middle| \sum_{i=k+1}^{n} x_i(t_m^+) + (k-1)x_k(t_m^+) > p_h \right\} \tag{66}$$

$$= \max \left\{ k \in \mathbb{N} \middle| \sum_{i=k}^{n-1} x_i(t_m) + (k-1)x_{k-1}(t_m) > p_h \right\}. \tag{67}$$

Using the definition

$$\Delta x_e = \frac{p_h - \sum_{j=\tilde{N}_d}^{n-1} x_j(t_m)}{\tilde{N}_d - 1}, \tag{68}$$

we find

$$t_{m+1} = t_m + \frac{\Delta x_e}{\mu} \tag{69}$$

and finally

$$x_i(t_{m+1}) = \begin{cases} p_h & \text{for } i = 1, \\ x_i(t_m^+) - \Delta x_e & \text{for } i = 2 \ldots \tilde{N}_d, \\ 0 & \text{for } i > \tilde{N}_d. \end{cases} \tag{70}$$

Collecting the pieces together, (65), (70), and (58) define the Poincaré map P^n of (57) for general n. In the following we will explicitly examine the case P^3.

In the limiting case of $p_h = 0$ no tank has to wait for filling. We obtain a switched arrival system[30] and the Poincaré map can be written explicitly as

$$\mathbf{x}(t_{m+1}) = M^{\mathrm{TII}}\mathbf{x}(t_m) + \min\left[x_1(t_m), x_{n-1}(t_m)\right] \begin{pmatrix} n-1 \\ -1 \\ \vdots \\ -1 \end{pmatrix}. \tag{71}$$

As shown in ref. 60 this system is chaotic for all $n > 2$ and has a constant invariant probability measure.

4.4. Bifurcation Analysis for $n = 3$

In the case $n = 3$, the Poincaré section B^3 in (56) is one-dimensional, and we have for $\mathbf{x} \in B^3$ the conditions $x_3 = 0$, $x_1 \in [p_h, L_h]$ and $x_2 = L_h - x_1$ (cf. Fig. 30). Thus we may parametrize B^3 by the coordinate x_1, and the Poincaré map is fully determined by a one-dimensional map

$$P^3 : [p_h, L_h] \to [p_h, L_h], \quad x_1(t_m) \mapsto x_1(t_{m+1}), \tag{72}$$

which we will now determine explicitly.

Following (58) we find:

$$x_1(t_m^+) = 0, \tag{73}$$

$$x_2(t_m^+) = \max\left[x_1(t_m), x_2(t_m)\right] = \max\left[x_1(t_m), L_h - x_1(t_m)\right], \tag{74}$$

$$x_3(t_m^+) = \min\left[x_1(t_m), L_h - x_1(t_m)\right], \tag{75}$$

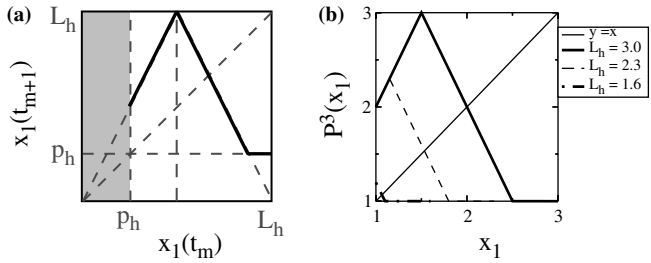

Fig. 31. (a) Schematic graph of the one-dimensional Poincaré map P^3 for the $n=3$ tank model according to Eq. (79). In the shaded region the map is not defined. (b) Graph of P^3 for $p_h=1$ and various values of L_h.

and condition (63) can be written as

$$2\,(L_h - x_1(t_m)) > p_h. \tag{76}$$

In the case that (76) is fulfilled we have from (65)

$$x_1(t_{m+1}) = 2\min\left[x_1(t_m),\, L_h - x_1(t_m)\right] \tag{77}$$

and otherwise $x_1(t_{m+1}) = p_h$.

Thus we may summarize the resulting Poincaré map in the case $n=3$ by

$$P^3 : [p_h, L_h] \to [p_h, L_h] \tag{78}$$

$$P^3(x_1) = \begin{cases} 2x_1 & \text{for } x_1 \in \left[p_h,\, \tfrac{1}{2}L_h\right) \\ 2L_h - 2x_1 & \text{for } x_1 \in \left[\tfrac{1}{2}L_h,\, L_h - \tfrac{1}{2}p_h\right) \\ p_h & \text{for } x_1 \in \left[L_h - \tfrac{1}{2}p_h,\, L_h\right] \end{cases} \tag{79}$$

$$= \max\left\{\left(L_h - |L_h - 2x_1|\right),\, p_h\right\}. \tag{80}$$

The graph of this map is schematically drawn in Fig. 31(a) and for various values of L_h in Fig. 31(b).

The dynamics of the iterated map (79) depends on the two positive[6] parameters p_h and L_h. The numerically calculated bifurcation diagram of $P^3(x_1)$ for fixed p_h and increasing L_h is shown in Fig. 32. We see that we recover a bifurcation structure which is very similar to the front model at low L_h (cf. Fig. 25). At any point with the same L_h/p_h both bifurcation

[6]Similar maps with negative p_h have been considered in ref. 65.

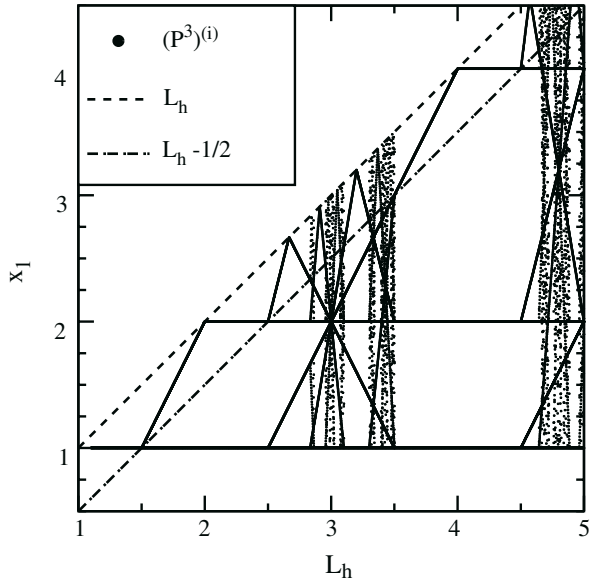

Fig. 32. Bifurcation diagram of the Poincaré map P^3 according to (79) for fixed $p_h = 1$ and varying L_h. Starting from a random $x_1^0 \in [p_h, L_h]$ we calculate at each L_h the ith iteration $x_1^i = P^3(x_1^{i-1})$. The plotted points are $x_1^{200} \ldots x_1^{300}$. The dashed and dash-dotted lines denote the left and right boundaries of the flat region of P^3, respectively.

diagrams show the same periodicity. This is not surprising, since the only necessary condition in the derivation of the tank model was that no fronts should reach the collector (see (47)). The nature of the bifurcations was not affected. However, the meaning of the variables has changed. While in Fig. 25 the positions of the collisions is plotted, Fig. 32 shows the size of the high field domain, when it is detached from the emitter. The information about the position of the collisions was lost in the derivation of the tank model, when the number of system variables was reduced from $2n-1$ to n.

4.4.1. Connection with the Flat-Topped Map

One-dimensional iterated maps are usually defined on the unit interval [0, 1]. This requirement may be met by an expansion of the domain of P^3 to $[0, L_h]$ followed by a rescaling off all lengths in units of L_h:

$$P^3(x_1) = L_h \hat{P}^3_{(p_h/L_h)} \left(\frac{x_1}{L_h} \right), \tag{81}$$

$$\hat{P}_z^3(x) = \begin{cases} 2x & \text{for } x \in \left[0, \frac{1}{2}\right), \\ 2-2x & \text{for } x \in \left[\frac{1}{2}, 1-\frac{1}{2}z\right), \\ z & \text{for } x \in \left[1-\frac{1}{2}z, 1\right]. \end{cases} \tag{82}$$

The flat segment of the map $\hat{P}_z^3(x)$ is located at the right edge of its domain in the interval $I_z^P = [1-z/2, 1]$ (cf. Fig. 33(a)). In the mathematical and physical literature, however, a slightly different class of *flat-topped* or *trapezoidal* maps of the form (see Fig. 33(b))

$$f_\lambda(x) = \min\left[1-|2x-1|, \lambda\right] \quad \text{for } \lambda \in [0, 1] \tag{83}$$

has been studied extensively.[66–68] The bifurcation diagram for this map is shown in Fig. 34(a). Here the flat segment is at the maximum of the map in the interval

$$I_\lambda^f = [\lambda/2, 1-\lambda/2] = \left[\frac{1}{2} - \frac{1-\lambda}{2}, \frac{1}{2} + \frac{1-\lambda}{2}\right]. \tag{84}$$

The boundaries of I_λ^f are indicated by dashed lines in Fig. 34(a).

We observe that by choosing

$$\lambda = 1 - \frac{z}{2} = 1 - \frac{p_h}{2L_h} \tag{85}$$

the flat segment of f_h is exactly the preimage of the flat segment of $\hat{P}_z^3$, i.e.

$$I_\lambda^f = \left(\hat{P}_z^3\right)^{-1}\left(I_z^P\right). \tag{86}$$

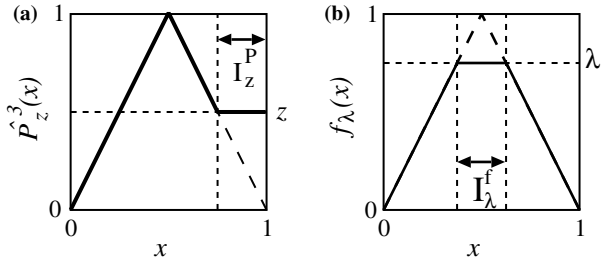

Fig. 33. Graphs of (a) $\hat{P}_z^3$ according to Eq. (82) and (b) $f_\lambda(x)$ according to Eq. (83).

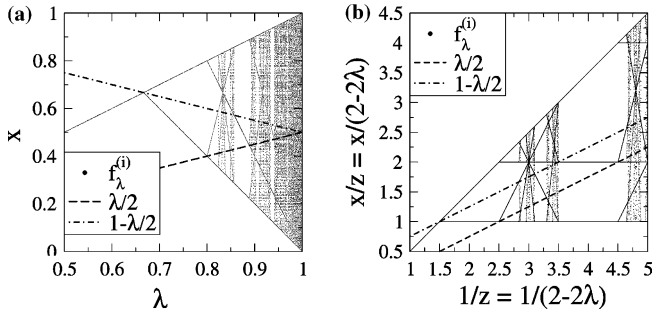

Fig. 34. Bifurcation diagrams of the flat topped map $f_\lambda(x)$ [cf. Eq. (83) and Fig. 33(b)]. The dashed and dash-dotted lines show the left and right boundaries of I_λ^f (84). Note that the left and right panels only differ in the axes scaling.

Consider now the two trajectories $x^1, x^2, x^3, \ldots$ and $y^1, y^2, y^3, \ldots$ of some initial point $x^0 = y^0 \notin I_z^P$, with $x^i = \hat{P}_z^3(x^{i-1})$ and $y^i = f_\lambda(y^{i-1})$. Let m be the first index, such that $x^m \in I_z^P$. From (86) we conclude that the first index n for which $x^n \in I_\lambda^f$, is given by $n = m-1$. Therefore the two trajectories y^i and x^i are identical for $i < m$. Since $y^{m-1} \in I_\lambda^f$ we have $y^m = \lambda$ and, using (85) we find $y^{m+1} = 2 - 2\lambda = z = x^{m+1}$. This means that the trajectories $x^1, x^2, x^3, \ldots$ and $y^1, y^2, y^3, \ldots$ only differ at indices m with $x^m \in I_z^P$, where we have $y^m = \lambda$. Apart from this difference, all other properties of the two trajectories such as periodicity or stability are identical. Hence we may restrict ourselves to the consideration of the *unimodal* map f_λ, which completely reproduces the bifurcation scenario of P^3.

This equivalence can also be seen directly from the bifurcation diagram of P^3 in Fig. 32. For any L_h there is only one point in the interval between the dashed and the dash-dotted line. If we map this point to the dash-dotted line, we obtain exactly the appropriately scaled bifurcation diagram of f_λ in Fig. 34(b).

4.4.2. The Tent Map Case $\lambda = 1$

For $\lambda = 1$ (i.e. $L_h \to \infty$ according to Eq. (85)), the function $f_1(x)$ in Eq. (82) reduces to the well known *tent map*

$$f_1(x) = 1 - |2x - 1|\,. \tag{87}$$

The tent map is an archetype of a chaotic map[69] that can be treated analytically. The results for this special case turn out to be useful in the discussion of the more complicated case $\lambda < 1$ (see Section 4.4.3).

The kth iterate of f_1, which we denote by $f_1^{(k)}$ has 2^k branches and is given by

$$f_1^{(k)}(x) = 1 - 2^k \left| x - \frac{2l+1}{2^k} \right| \quad \text{for } x \in \left[\frac{l}{2^{k-1}}, \frac{l+1}{2^{k-1}} \right], \; l = 0 \ldots 2^{k-1} - 1. \tag{88}$$

The fixed points of $f_1^{(k)}$, which are the points of period k, are explicitly given by

$$\begin{aligned} p_l^{(k)} &= \frac{2l}{2^k - 1} \\ n_l^{(k)} &= \frac{2l+2}{2^k + 1} \end{aligned} \qquad \text{for } l = 0 \ldots 2^{k-1} - 1. \tag{89}$$

The slopes of $f_1^{(k)}(x)$ at the fixed points are given by $\partial_x f_1^{(k)}(p^{(k)}) = 2^k$ and $\partial_x f_1^{(k)}(n^{(k)}) = -2^k$. Thus all fixed points are unstable, which means that the tent map f_1 has no stable periodic orbits. The dynamics is chaotic[70] and has a constant invariant measure.[7] Furthermore it follows that

$$f_1^{(k)}(x) > x \quad \text{for } x \in [p_l^{(k)}, n_l^{(k)}], \quad l = 0 \ldots 2^{k-1} - 1. \tag{90}$$

In Fig. 35 the iterates $f_1^{(k)}$, and the fixed points $p_l^{(4)}$ and $n_l^{(4)}$ for $k = 4$ are depicted.

It is worthwhile to note that the fixed points $x_l^{(k)}$ follow a remarkable pattern, when written in binary notation. The variable l in (89) can be written as a binary number $l = \%Q$, where Q is a string consisting of $k-1$ letters of 0 or 1 (we fill up with leading 0s as necessary) and the % indicates a binary number. We denote by $\tilde{Q}$ the bitwise inverse of Q (i.e. $\%\tilde{Q} = 2^k - \%Q$). A few lines of algebra show that the fixed points in (89) are given in the binary number base by

$$\begin{aligned} p_l^{(k)} &= p_Q^k = \%0.Q0Q0Q0Q0Q\ldots \\ n_l^{(k)} &= n_Q^k = \%0.Q1\tilde{Q}0Q1\tilde{Q}0Q\ldots \end{aligned} \qquad \text{for } l = \%Q = 0 \ldots 2^{k-1} - 1. \tag{91}$$

[7] Formally, there are infinitely many fixed points of the Perron Frobenius operator for f_1, but only the constant measure is natural, in the sense that it is stable against fluctuations (see Exercise 7.5 in ref. 69).

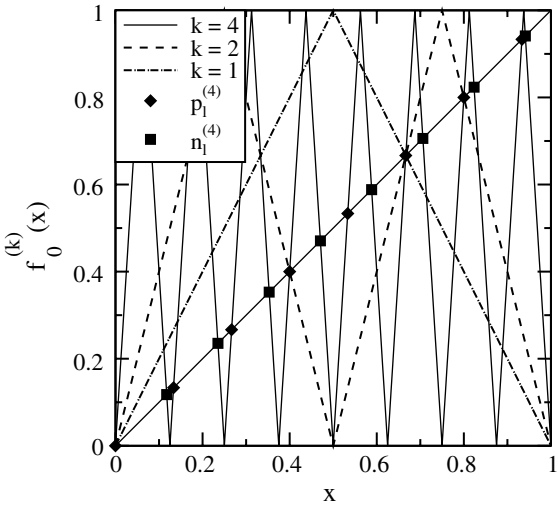

Fig. 35. Iterations of the tent map $f_0^{(k)}$ for various k according to Eq. (88), and fixed points $p_1^{(k)}$ and $n_1^{(k)}$ according to Eq. (89).

The appearance of the patterns in (91) is also directly explained by considering the tent map (87) in binary notation,[69]

$$f_1(\%0.X) = \begin{cases} \%0.Y & \text{for } X = 0Y, \\ \%0.\tilde{Y} & \text{for } X = 1Y. \end{cases} \tag{92}$$

For $f_1^{(k)}$ we then find

$$f_1^{(k)}(\%0.X) = \begin{cases} \%0.Y & \text{for } X = Q0Y \\ \%0.\tilde{Y} & \text{for } X = Q1Y. \end{cases} \quad \text{for } \%Q = 0 \ldots 2^{k-1} - 1 \tag{93}$$

and requiring $X = Y$ or $X = \tilde{Y}$ yields directly the patterns for p_Q^k or n_Q^k of Eq. (89), respectively.

4.4.3. The Case $\lambda < 1$

In order to finally explain the bifurcation scenarios in Fig. 32, we now want to characterize the stable periodic trajectories of f_λ. In the following we will discuss the trajectory of $x_\lambda^0 = 1/2$ given by

$$x_\lambda^1, x_\lambda^2, x_\lambda^3, \ldots \quad \text{with } x_\lambda^k = f_\lambda\left(x_\lambda^{k-1}\right) \text{ and } x_\lambda^1 = f_\lambda\left(\frac{1}{2}\right). \tag{94}$$

From (84) we see that $x_\lambda^0 = 1/2 \in I_\lambda^f$ and thus $x_\lambda^1 = \lambda$. Let $k = k(\lambda)$ be the first index with $x_\lambda^k \in I_\lambda^f$ and let us assume that[8] $k < \infty$. Then $x_\lambda^{k+1} = \lambda$ and the trajectory (94) has period $k(\lambda)$. Since $\partial_x f(x^k) = 0$ we find

$$\frac{\partial f_\lambda^{(k)}(x_\lambda^i)}{\partial x} = \prod_{j=i}^{i+k-1} \frac{\partial f_\lambda(x_\lambda^j)}{\partial x} = 0 \quad \text{for } i \leqslant k \tag{95}$$

and the trajectory $x_\lambda^1, \ldots, x_\lambda^k$ is a stable period $k(\lambda)$ orbit.

We now want to determine the function $k(\lambda)$. This can in principle be done, by considering the iterates $f_\lambda^{(j)}$, but this approach is analytically quite involved. Instead, we make use of the known iterates $f_1^{(j)}$ of the tent map (see Eq. (88)). Since f_λ differs from the tent map f_1 only in the interval I_λ^f, and $x_\lambda^i \notin I_\lambda^f$ for $1 < i < k$, we may write

$$x_\lambda^i = f_1^{(i-1)}(\lambda), \quad \text{for } 1 < i \leqslant k. \tag{96}$$

The condition $x_\lambda^k \in I_\lambda^f$ for a stable period k orbit, can then be rephrased in term of the tent map as $f_1(x_\lambda^k) \geqslant f_\lambda(x_\lambda^k) = \lambda$. Formally we may thus express $k(\lambda)$ as

$$k(\lambda) = \min\left\{ i \in \mathbb{N} \middle| f_1^{(i)}(\lambda) \geqslant \lambda \right\}. \tag{97}$$

This formula allows for a simple "graphical" interpretation with the help of Fig. 35. To find $k(\lambda)$, choose the point (λ, λ) on the diagonal, and find the smallest k, such that $f_1^{(k)}$ is above the diagonal. In this way, we may for instance find $k(\lambda) = 4$ for $\lambda \in [p_6^{(4)}, n_6^{(4)}]$. In the following we will show that all intervals with fixed k are of this form.

Let us now consider the trajectories of x_λ^i under variation of λ. Applying the chain rule to (96) yields

$$\frac{\partial x_\lambda^i}{\partial \lambda} = a(-1)^{N_R(i)} 2^{[(i-1) \bmod k]}, \tag{98}$$

[8]It was shown in ref. 66 that the set $\{\lambda | k(\lambda) \to \infty\}$ has Lebesgue measure zero.

where

$$N_R(i) = a\left|\left\{ j \,\middle|\, x_\lambda^j > \frac{1}{2} \wedge 1 \leqslant j \leqslant [(i-1) \bmod k] \right\}\right| \tag{99}$$

and $|\cdot|$ denotes the cardinal number. Here N_R counts the number of minus signs that are picked up by visiting the negative slope region of f_1. The bifurcation parameter λ only enters implicitly in the right-hand side of Eq. (98) via $k(\lambda)$. Let us for example consider a λ range, for which a minimal k_0 exists, such that $k_0 \leqslant k(\lambda)$. Then we have $x_\lambda^i \notin I_\lambda^f$ for $i < k_0$, and $N_R(i)$ in (99) will be constant across the considered λ range. Thus x_λ^i for $i \leqslant k_0$ will depend linearly on λ by Eq. (98). This naturally explains the appearance of the straight lines in Fig. 34(a) even across complicated bifurcations. These straight lines are preserved under the axis transformation leading to Fig. 34(b). We can now also explain the appearance of the cobweb structures, for instance at $\lambda_c = 5/6$ [cf. $1/z = 3$ in Fig. 34(b)]. This yields a trajectory with $x_\lambda^i = 2/3$ for $i \geq 2$. Thus $k(\lambda_c)$ formally diverges, and we can find intervals around λ_c with arbitrary high k_0. Therefore the points x_λ^k for $2 \geqslant k \leqslant k_0$ will converge in straight lines to $x_\lambda^k \to 2/3$ for $\lambda \to \lambda_c$. This explains the typical cobweb structure, where bundles of straight lines appear to converge in a single point.

Due to (98), the point $x_\lambda^k \in I_\lambda^f$ has the largest absolute slope with respect to λ of all points in the trajectory $x_\lambda^0, \ldots, x_\lambda^k$. Bifurcations, i.e. a change in $k(\lambda)$, will only appear, if either with increasing λ the point x_λ^k leaves I_λ^f, or another point x_λ^i with $i < k$ enters I_λ^f. This latter case is not independent from the first one, since for any λ, there cannot exist simultaneously two distinct points x_λ^i, x_λ^k in I_λ^f. Since x_λ^k moves continuously, it must leave I_λ^f as x_λ^i enters it. With the help of (97) and (90) we infer that the bifurcation points are fixed points of $f_1^{(k)}$, and that the intervals with constant $k(\lambda)$ are of the form (see (91))

$$I_Q^k = \left[p_Q^k, n_Q^k \right] \tag{100}$$

with a *suitable* binary string Q of length $k-1$. Suitable in this context means that

$$f_1^{(i)}(\lambda) \leqslant \lambda \quad \text{for all } \lambda \in I_Q^k \text{ and } i < k. \tag{101}$$

The question is now, how to construct those suitable Q. The following construction is essentially analogous to the classical construction of the universal U-sequences[71] and will finally result in Table II, where all Qs

Table II. Intervals with Constant Period up to Period 7 (with the Exception of the Period 8 Pattern in Line 4)

Number	k	Q	p_Q^k	n_Q^k	Itinerary
1	1	Empty	0	$0.\overline{10}$	Empty
2	2	1	$0.\overline{10}$	$0.\overline{1100}$	R
3	4	110	$0.\overline{1100}$	$0.\overline{11010010}$	RLR
4	8	1101001	$0.\overline{11010010}$	$0.\overline{1101001100101100}$	RLR^3LR
5	6	11010	$0.\overline{110100}$	$0.\overline{110101001010}$	RLR^3
6	7	110101	$0.\overline{1101010}$	$0.\overline{11010110010100}$	RLR^4
7	5	1101	$0.\overline{11010}$	$0.\overline{1101100100}$	RLR^2
8	7	110110	$0.\overline{1101100}$	$0.\overline{11011010010010}$	RLR^2LR
9	3	11	$0.\overline{110}$	$0.\overline{111000}$	RL
10	6	11100	$0.\overline{111000}$	$0.\overline{111001000110}$	RL^2RL
11	7	111001	$0.\overline{1110010}$	$0.\overline{11100110001100}$	RL^2RLR
12	5	1110	$0.\overline{11100}$	$0.\overline{1110100010}$	RL^2R
13	7	111010	$0.\overline{1110100}$	$0.\overline{11101010001010}$	RL^2R^3
14	6	11101	$0.\overline{111010}$	$0.\overline{111011000100}$	RL^2R^2
15	7	111011	$0.\overline{1110110}$	$0.\overline{11101110001000}$	RL^2R^2L
16	4	111	$0.\overline{1110}$	$0.\overline{11110000}$	RL^2
17	7	111100	$0.\overline{1111000}$	$0.\overline{11110010000110}$	RL^3RL
18	6	11110	$0.\overline{111100}$	$0.\overline{111101000010}$	RL^3R
19	7	111101	$0.\overline{1111010}$	$0.\overline{11110110000100}$	RL^3R^2
20	5	1111	$0.\overline{11110}$	$0.\overline{1111100000}$	RL^3
21	7	111110	$0.\overline{1111100}$	$0.\overline{11111010000010}$	RL^4R
22	6	11111	$0.\overline{111110}$	$0.\overline{111111000000}$	RL^4
23	7	111111	$0.\overline{1111110}$	$0.\overline{11111110000000}$	RL^5

up to period 7 are listed. Here we have the advantage that in our case all intervals can be calculated explicitly, and we can avoid symbolic dynamics in the derivation, but in hindsight we see that symbolic arguments yield essentially the same results. We stress that the U-sequence is different from the well known Sarkovskii ordering,[70,72] since the latter is only a statement about the existence of periods, and not about their stability. The U-sequence however predicts the exact sequence of all stable periods, as one bifurcation parameter is changed.

4.4.4. Elementary Intervals

The most elementary strings Q, which fulfill the condition (101) are simply of the form

$$Q^k = \underbrace{1 \dots 1}_{k-1} = 1^{k-1}, \tag{102}$$

where we have used a convenient exponential notation a^b, i.e. a b-fold repetition of the letter a. Then we have from (100),

$$I^k_{Q^k} = [\%0.1^{k-1}01^{k-1}0 \dots, \%0.1^k0^k1^k0^k \dots], \tag{103}$$

which means that any $\lambda \in I^k_{Q^k}$ is of the form $\lambda = \%0.1^{k-1}X$ with $\%0.\tilde{X} \leqslant \lambda$. Consequently, by

$$f_1^{(i)}(\lambda) = 0.0^{k-i-1}\tilde{X} \leqslant \lambda \quad \text{for } 1 \leqslant i < k, \tag{104}$$

condition (101) is fulfilled. On the other hand $f_1^k(\lambda) \geqslant \lambda$ by construction (cf. (90)) and thus for $\lambda \in I^k_{Q^k}$, we have indeed a stable period k orbit. This construction yields the rows #1, 2, 9, 16, 20, 22, 23 of Table II.

4.4.5. Period Doubling Cascade

The next basic bifurcation scenario is the period doubling of any given suitable pattern Q_1. Assume that Q_1 fulfills (101) and consider the interval $I^{2k}_{Q_2}$ with Q_2 being the harmonic extension of Q_1 defined by

$$Q_2 = H(Q_1) = Q_1 1 \tilde{Q}_1. \tag{105}$$

Then the boundaries of $I^{2k}_{Q_2}$ are of the form

$$p^{2k}_{Q_2} = \%0.Q_20Q_20Q_20 \dots = \%0.Q_11\tilde{Q}_10Q_11\tilde{Q}_10Q_11\tilde{Q}_10 = n^k_{Q_1}, \tag{106}$$

$$n^{2k}_{Q_2} = \%0.Q_21\tilde{Q}_20Q_21\tilde{Q}_20 \dots = \%0.Q_11\tilde{Q}_11\tilde{Q}_10Q_10Q_11\tilde{Q}_11\tilde{Q}_10Q_10 \dots \tag{107}$$

The interval $I^{2k}_{Q_2}$ therefore connects consecutively to $I^k_{Q_1}$ from the right, with only the boundary point in common.

We now want to show that $I^{2k}_{Q_2}$ fulfills the condition (101). Assume that Q_2 would not fulfill (101), i.e. we can find a $\lambda \in I^{2k}_{Q_2}$ and $i < 2k$, such that $f_1^{(i)}(\lambda_i) > \lambda_i$. Since $f_1^{(i)}(n^k_{Q_1}) \leqslant n^k_{Q_1}$ we find by continuity $\lambda_0 \in I^k_{Q_1}$ with

$f_1^{(i)}(\lambda_f)=\lambda_f$. This λ_f is then also a fixed point of $f_1^{(2i)}, f_1^{(3i)}, \ldots$. In particular, we may choose $j=mi$, such that $k \leqslant j < 2k$, and will find a

$$\lambda_j \in I_{Q_1}^k \quad \text{with } f_1^{(j)}(\lambda_j) > \lambda_j \text{ and } k \leqslant j < 2k. \tag{108}$$

Since

$$f_1^{(k)}(p_{Q_2}^{2k}) = n_{Q_1}^k \in I_{Q_1}^k, \tag{109}$$

$$f_1^{(k)}(n_{Q_2}^{2k}) = \%0.Q_1 0 Q_1 1 \tilde{Q}_1 \ldots \in I_{Q_1}^k \tag{110}$$

we have

$$f_1^{(k)}(I_{Q_2}^{2k}) \subset I_{Q_1}^k \tag{111}$$

and in particular $f^{(k)}(\lambda_j) \in I_{Q_1}^k$. By (108) we infer that $f^{(j-k)}(f^{(k)}(\lambda_j)) > n_{Q_1}^k$, but this is not possible, since it would contradict the assumption that Q_1 fulfills the condition (101). Thus Q_2 must also fulfill the condition (101), and $I_{Q_2}^{2k}$ is a suitable interval. This argument can be repeated for $Q_3 = H(Q_2)$, etc. leading to a classical period doubling cascade.

We can now apply the period doubling construction to all patterns Q^k found in Section 4.4.4. This yields the lines #2, 3, 4, 10 of Table II.

The first period doubling starting with the empty string $Q^1 = Q_1$ was also studied by different methods in Ref. 68. It was found that the Feigenbaum parameter δ, which is the ratio of two subsequent intervals in the period doubling cascade is not constant but scales as

$$\delta(k) = 2^k. \tag{112}$$

Since k itself obviously doubles at every period doubling, this yields an exponentially fast convergence of the sequence of bifurcation points.

4.4.6. Intermediate Intervals

We now want to recursively construct the remaining Qs of Table II. Assume that we are given an ordered list of all intervals $I_{Q_i}^{k_i}$ up to a certain period $k_{\max}$ and let Q_A and Q_B be two strings characterizing two neighboring intervals $I_{Q_A}^{k_A}$ and $I_{Q_B}^{k_B}$ with $n_{Q_A}^{k_A} < p_{Q_B}^{k_B}$ (which implies that

$Q_B \neq H(Q_A)$). Let us then consider the following common substring Q, given by

$$n_{Q_A}^{k_A} = \%0.Q0X_A, \tag{113}$$

$$p_{Q_B}^{k_B} = \%0.Q1X_B. \tag{114}$$

We then see immediately that $p_Q^k < p_{Q_B}^{k_B}$ and $n_Q^k > n_{Q_A}^{k_A}$. Thus the interval I_Q^k is between the intervals $I_{Q_A}^{k_A}$ and $I_{Q_B}^{k_B}$, but since we assumed that we had started with a complete list up to period $k_{\max}$, it follows that $k > k_{\max}$, and Q is a suitable string in the sense of (101). Applying this construction repeatedly to all pairs of neighboring intervals, we can construct new lists with larger and larger $k_{\max}$. This finally yields all remaining lines in Table II. With this construction we have thus explicitly calculated the bifurcation points of the map f_λ, and at the same time solved the original bifurcation problem of P^3. We know now the exact sequence of periodic orbits as λ, or in the case of P^3, the parameter L_h increases. Up to about period seven this sequence can be readily confirmed by the microscopic model (cf. Fig. 21).

4.4.7. Symbolic Dynamics

At this point we are able to tie up the present study with the subject of *symbolic dynamics*, which since the classical work of Metropolis, Stein and Stein[71] has developed into a powerful tool in the study of universal features in nonlinear systems.[69,66,73]

Let us consider the trajectory x_λ^i of the tent map and write a string, $M_\lambda = X_1 X_2 X_3 \ldots$ with letters

$$X_i = \begin{cases} L & \text{for } x^i < 1/2, \\ R & \text{for } x^i \geqslant 1/2. \end{cases} \tag{115}$$

Instead of dealing with the explicit binary representation of λ, one can now use the itinerary M_λ instead, since it can be shown that there exists a one to one correspondence between the two representations.[69] The advantage of the itinerary approach is that it is applicable to a large class of one dimensional maps, although the construction of Table II is less explicit and intuitive.[71] Comparing the itineraries in Table II with the Table in the appendix of ref. 71, however, shows that both approaches are indeed equivalent.

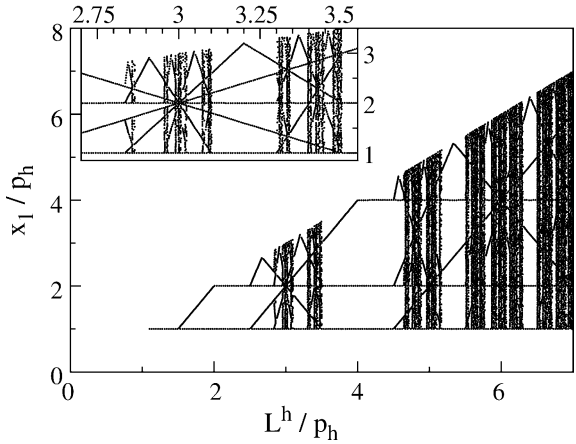

Fig. 36. Bifurcation diagram as in Fig. 32, but for the map (79) with a flat region modified by a finite slope $m = 0.001$ (cf. Fig. 33).

4.4.8. Chaoticity

The maps P^3 and f_λ we have considered in the previous sections show rich bifurcation scenarios, with infinitely long periods, which we can now explain sufficiently well by means of the U-sequences. Nevertheless they are not truly chaotic. The reason is obviously the flat segment, which will eventually be reached by the trajectory, and will render any orbit stable. Such flat segments are, however, not physical, since they would correspond to an exact projection of a continuous set of phase points onto one single phase point. Since in the derivation of the tank model, a number of approximations were made, it is more likely that the flat segment is not exactly flat, but has at least a tiny slope $0 < m \ll 1$. Since this finite slope increases in the iterated map as $2^k m$, it will destabilize periodic orbits of period $k(\lambda) > \log(1/m)$ and result in chaotic behavior. As shown in Fig. 36, this leads to continuous bands similar to the ones observed in the microscopic model (cf. Fig. 21).

5. CONCLUSION

We have studied a system consisting of interacting moving fronts, which is derived from the microscopic description of a semiconductor superlattice. One reason for this interest in superlattices can be attributed to the expected technological applicability, for instance in Terahertz electronics, but from a more fundamental point of view, the significance of the superlattice as a nonlinear model system, is equally important.

We have based our analysis on a semiclassical sequential tunneling model for the electrons, which is motivated by quantum mechanical considerations. The resulting nonlinear transport equations give rise to the formation of electron accumulation and depletion fronts, which form the boundaries between high- and low-field domains. It is thus natural to look for a description of the superlattice dynamics in terms of fronts. Such a front model provides a new hierarchical level on top of the semiclassical model.

We have studied the propagation, generation and annihilation of single fronts in detail. It was found in Section 2 that the front velocities are determined by the overall current density, while the generation of fronts at the emitter is governed by the nature of the emitter contact, characterized by the contact conductivity σ. Fronts disappear from the system, as they either reach the collector, or collide with a front of opposite polarity. It is this latter possibility of front annihilation that allows for particularly interesting scenarios, such as chaotic behavior under fixed external voltage conditions.

We have demonstrated in Section 3 that large parts of the bifurcation scenarios of the microscopic model can be reproduced by a model which uses the front positions as the dynamical variables. This front model has a very generic structure, and it may be relevant for other systems with front dynamics under global constraints as well.

As shown in Section 4, a further simplification of the front model applies if the fronts do not reach the collector. In this case the front model maps to a tank model, which describes the filling heights of a number of water tanks. The tanks are filled and drained by a given set of rules. Similar models are obtained generically in various areas of science and engineering, for instance in the context of production processes. The tank model can be described analytically in terms of iterated maps. In Section 4 we have explicitly constructed the maps for the first nontrivial case $n = 3$, and derived explicitly the universal U-sequence for the stable periods. The same U-sequence appears in a large class of one-dimensional iterated maps. This finally explains the peculiar bifurcation scenario observed in the microscopic model.

ACKNOWLEDGMENT

We thank A. Wacker for many fruitful discussions. Helpful discussions with M. Abel, L. Bonilla, N. Janson, K. Peters, U. Parlitz and J. Schlesner are also acknowledged. This work was supported by DFG in the framework of Sfb 555.

REFERENCES

1. A. Scott (ed.), Encyclopedia of Nonlinear Science (Routledge, London, 2005).
2. J. S. Langer, Instabilities and pattern formation in crystal growth, *Rev. Mod. Phys*. **52**:1 (1980).
3. B. Boroson, R. McCray, C. O. Clark, J. Slavin, M.-M. M. Low, Y.-H. Chu, and D. V. Buren, An interstellar conduction front within a wolf-rayet ring nebula observed with the GHRS, *Astrophys J.* **478**:638 (1997).
4. A. M. Zhabotinskii, Periodic processes of the oxidation of malonic acid in solution, *Biofizika* **9**:306 (1964).
5. R. Kapral and K. Showalter (ed.), Chemical Waves and Patterns (Kluwer Academic Publishers, Dordrecht, 1995).
6. A. G. Merzhanov and E. N. Rumanov, Physics of reaction waves, *Rev. Mod. Phys*. **71**:1173 (1999).
7. J. M. Davidenko, A. M. Pertsov, R. Salomonsz, W. Baxter and J. Jalife, Stationary and drifting spiral waves of excitation in isolated cardiac muscle, *Nature* **355**:349 (1992).
8. O. Steinbock, F. Siegert, S. C. Müller, and C. J. Weijer, Three-dimensional waves of excitation during dictyostelium morphogenesis, *Proc. Natl. Acad. Sci*. **90**:7332 (1993).
9. M. C. Cross and P. C. Hohenberg, Pattern formation outside of equilibrium, *Rev. Mod. Phys*. **65**:851 (1993).
10. A. S. Mikhailov, Foundations of Synergetics *Vol. I* 2nd ed. (Springer, Berlin, 1994),
11. G. Falkovich, K. Gawdzki and M. Vergassola, Particles and fields in fluid turbulence, *Rev. Mod. Phys.* **73**:913 (2001).
12. J. B. Gunn, Microwave oscillations of current in III-V semiconductors, *Sol. Stat. Comm.* **1**:88 (1963).
13. V. L. Bonch-Bruevich, I. P. Zvyagin, and A. G. Mironov, Domain Electrical Instabilities in Semiconductors (Consultant Bureau, New York, 1975).
14. E. Schöll, Nonequilibrium Phase Transitions in Semiconductors (Springer, Berlin, 1987).
15. M. P. Shaw, V. V. Mitin, E. Schöll, and H. L. Grubin, The Physics of Instabilities in Solid State Electron Devices (Plenum Press, New York, 1992).
16. J. Peinke, J. Parisi, O. Rössler, and R. Stoop, Encounter with Chaos (Springer, Berlin, Heidelberg, 1992).
17. E. Schöll, F.-J. Niedernostheide, J. Parisi, W. Prettl, and H. Purwins, Formation of Spatio-temporal structures in semiconductors, in *Evolution of spontaneous structures in Dissipative Continuous Systems*, F. H. Busse and S. C. Müller (Springer, Berlin, 1998), pp. 446–494.
18. K. Aoki, Nonlinear Dynamics and Chaos in Semiconductors (Institute of Physics Publishing, Bristol, 2000).
19. E. Schöll, Nonlinear Spatio-temporal Dynamics and Chaos in Semiconductors. Nonlinear Science Series, Vol. 10 (Cambridge University Press, Cambridge, 2001).
20. I. R. Cantalapiedra, M. J. Bergmann, L. L. Bonilla, and S. W. Teitsworth, Chaotic motion of space charge wave fronts in semiconductors under time independent voltage bias, *Phys. Rev. E* **63**:056216 (2001).
21. L. L. Bonilla and I. R. Cantalapiedra, Universality of the Gunn effect, Self-sustained oscillations mediated by solitary waves, *Phys. Rev. E* **56**:3628 (1997).
22. A. Wacker, Semiconductor superlattices: A model system for nonlinear transport, *Phys. Rep.* **357**:1 (2002).
23. L. L. Bonilla, Theory of nonlinear charge transport, wave propagation, and self-oscillations in semiconductor superlattices, *J. Phys.: Condens. Matter* **14**:R341 (2002).

24. E. Schomburg, R. Scheuerer, S. Brandl, K. F. Renk, D. G. Pavel'ev, Y. Koschurinov, V. Ustinov, A. Zhukov, A. Kovsh, and P. S. Kop'ev, InGaAs/InAlAs superlattice oscillator at 147 GHz, *Electron. Lett.* **35**:1491 (1999).
25. J. Schlesner, A. Amann, N. B. Janson, W. Just, and E. Schöll, Self-stabilization of high frequency oscillations in semiconductor superlattices by time–delay autosynchronization, *Phys. Rev. E* **68**:066208 (2003).
26. J. Schlesner, A. Amann, N. B. Janson, W. Just, and E. Schöll, Self-stabilization of chaotic domain oscillations in superlattices by time–delayed feedback control, *Semicond. Sci. Technol*. **19**:S34 (2004).
27. J. Faist, F. Capasso, D. L. Sivco, C. Sirtori, A. L. Hutchinson, and A. Y. Cho, Quantum cascade laser, Science **264**:553 (1994).
28. C. Gmachl, F. Capasso, D. L. Sivco, and A. Y. Cho, Recent progress in quantum cascade lasers and applications, *Rep. Prog. Phys*. **64**:1533 (2001).
29. T. M. Fromhold, A. Patane, S. Bujkiewicz, P. B. Wilkinson, D. Fowler, D. Sherwood, S. P. Stapleton, A. A. Krokhin, L. Eaves, M. Henini, N. S. Sankeshwar, and F. W. Sheard, Chaotic electron diffusion through stochastic webs enhances current flow in superlattices, *Nature* **428**:726 (2004).
30. C. Chase, J. Serrano, and P. J. Ramadge, Periodicity and chaos from switched flow systems: contrasting examples of discretely controlled continuous flow systems, *IEEE Trans. Automat. Control* **38**:70 (1993).
31. H. Steuer, A. Wacker, E. Schöll, M. Ellmauer, E. Schomburg, and K. F. Renk, Thermal breakdown, bistability, and complex high-frequency current oscillations due to carrier heating in superlattices, *Appl. Phys. Lett*. **76**:2059 (2000).
32. G. Grüner, The dynamics of charge-density waves, *Rev. Mod. Phys*. **60**:1129 (1988).
33. J. P. Keener and J. Sneyd, *Mathematical physiology* (Springer, New York, Berlin, 1998).
34. S. Flach, Y. Zolotaryuk, and K. Kladko, Moving lattice kinks and pulses: An inverse method, *Phys. Rev. E* **59**:6105 (1999).
35. A. Carpio and L. L. Bonilla, Depinning transitions in discrete reaction-diffusion equations, *SIAM J. Appl. Math*. **63**:1056 (2003).
36. L. L. Bonilla, M. Kindelan, M. Moscoso, and S. Venakides, Periodic generation and propagation of travelling fronts in dc voltage biased semiconductor superlattices, *SIAM J. Appl. Math*. **57**:1588 (1997).
37. A. Carpio, L. L. Bonilla, A. Wacker, and E. Schöll, Wavefronts may move upstream in semiconductor superlattices, *Phys. Rev. E* **61**:4866 (2000).
38. A. Amann, A. Wacker, L. L. Bonilla, and E. Schöll, Dynamic scenarios of multi-stable switching in semiconductor superlattices, *Phys. Rev. E* **63**:066207 (2001).
39. A. Carpio, L. L. Bonilla, and G. Dell'Acqua, Motion of wave fronts in semiconductor superlattices, *Phys. Rev. E* **64**:036204 (2001).
40. J. Kastrup, R. Hey, K. H. Ploog, H. T. Grahn, L. L. Bonilla, M. Kindelan, M. Moscoso, A. Wacker, and J. Galán, Electrically tunable GHz oscillations in doped GaAs-AlAs superlattices, *Phys. Rev. B* **55**:2476 (1997).
41. L. L. Bonilla, J. Galán, J. A. Cuesta, F. C. Martínez, and J. M. Molera: Dynamics of electric field domains and oscillations of the photocurrent in a simple superlattice model, *Phys. Rev. B* **50**:8644 (1994).
42. A. Amann, J. Schlesner, A. Wacker, and E. Schöll, Self-generated chaotic dynamics of field domains in superlattices, in Proc. of 26th International Conference on the Physics of Semiconductors (ICPS-26), (Edinburgh 2002), ed. J. H. Davies and A. R. Long (2003).
43. L. L. Bonilla, I. R. Cantalapiedra, G. Gomila, and J. M. Rubí, Asymptotic analysis of the Gunn effect with realistic boundary conditions, *Phys. Rev. E* **56**:1500 (1997).

44. D. Sánchez, M. Moscoso, L. L. Bonilla, G. Platero, and R. Aguado, Current self-oscillations, spikes and crossover between charge monopole and dipole waves in semiconductor superlattices, *Phys. Rev. B* **60**:4489 (1999).
45. J. Kastrup, F. Prengel, H. T. Grahn, K. Ploog, and E. Schöll, Formation times of electric field domains in doped GaAs-AlAs superlattices, *Phys. Rev. B* **53**:1502 (1996).
46. O. M. Bulashenko and L. L. Bonilla, Chaos in resonant-tunneling superlattices, *Phys. Rev. B* **52**:7849 (1995).
47. K. N. Alekseev, G. P. Berman, D. K. Campbell, E. H. Cannon, and M. C. Cargo, Dissipative chaos in semiconductor superlattices, *Phys. Rev. B* **54**:10625 (1996).
48. L. L. Bonilla, O. M. Bulashenko, J. Galán, M. Kindelan, and M. Moscoso, Dynamics of electric-field domains and chaos in semiconductor superlattices, *Sol. State El.* **40**:161 (1996).
49. O. M. Bulashenko, K. J. Luo, H. T. Grahn, K. H. Ploog, and L. L. Bonilla, Multifractal dimension of chaotic attractors in a driven semiconductor superlattice, *Phys. Rev. B* **60**:5694 (1999).
50. J. C. Cao and X. L. Lei, Synchronization and chaos in miniband semiconductor superlattices, *Phys. Rev. B* **60**:1871 (1999).
51. Y. Zhang, J. Kastrup, R. Klann, K. H. Ploog, and H. T. Grahn, Synchronization and chaos induced by resonant tunneling in GaAs/AlAs superlattices, *Phys. Rev. Lett.* **77**:3001 (1996).
52. K. J. Luo, H. T. Grahn, K. H. Ploog, and L. L. Bonilla, Explosive bifurcation to chaos in weakly coupled semiconductor superlattices, *Phys. Rev. Lett*. **81**:1290 (1998).
53. A. Amann, J. Schlesner, A. Wacker, and E. Schöll, Chaotic front dynamics in semiconductor superlattices, *Phys. Rev. B* **65**:193313 (2002).
54. M. Or-Guil, I. G. Kevrekidis, and M. Bär, Stable bound states of pulses in an excitable medium, *Physica D* **135**:154 (2000).
55. A. Wolf, J. Swift, H. Swinney, and J. Vastano, Determining Lyapunov exponents from a time series, *Physica D* **16**:285 (1985).
56. J. Schlesner and A. Amann, Superlattice bifurcation scenarios (2003), private communication.
57. A. Amann, K. Peters, U. Parlitz, A. Wacker, and E. Schöll: A hybrid model for chaotic front dynamics: From semiconductors to water tanks, *Phys. Rev. Lett*. **91**:066601 (2003).
58. R. Alur, C. Courcoubetis, N. Halbwachs, T. A. Henzinger, P.-H. Ho, X. Nicollin, A. Olivero, J. Sifakis, and S. Yovine, The algorithmic analysis of hybrid systems, *Theoretical Computer Science* **138**:3 (1995).
59. I. Katzorke and A. Pikovsky, Chaos and complexity in a simple model of production dynamics, *Discrete Dyn. Nature Soc.* **5**:179 (2000).
60. T. Schürmann and I. Hoffmann, The entropy of strange billards inside *n*-simplexes, *J. Phys. A* **28**:5033 (1995).
61. K. Peters and U. Parlitz, Hybrid systems forming strange billards, *Int. J. Bifur. Chaos* **13**:2575 (2003).
62. R. Carretero-González, D. K. Arrowsmith, and F. Vivaldi, One-dimensional dynamics for traveling fronts in coupled map lattices, *Phys. Rev. E* **61**:1329 (2000).
63. A. Torcini, A. Vulpiani, and A. Rocco, Front propagation in chaotic and noisy reaction-diffusion systems: a discrete-time map approach, *Eur. Phys. J. B* **25**:333 (2002).
64. L. Kleinrock, Queueing Systems (Wiley, New York, 1975).
65. O. Rudzick, A. Pikovsky, C. Scheffczyk, and J. Kurths: Dynamics of chaos-order interface in coupled map lattices, *Physica D* **103**:330 (1997).
66. K. M. Brucks, M. Misiurewicz, and C. Tresser, Monotonicity properties of the family of trapezoidal maps, *Commun. Math. Phys*. **137**:1 (1991).

67. L. Glass and W. Zeng, Bifurcations in flat-topped maps and the control of cardiac chaos, *Int. J. Bif. Chaos* **4**:1061 (1994).
68. C. Wagner and R. Stoop, Renormalization approach to optimal limiter control in 1-d chaotic systems, *J. Stat. Phys*. **106**:97 (2002).
69. P. Cvitanović, R. Artuso, R. Mainieri, G. Tanner, and G. Vattay, Chaos: Classical and Quantum (Niels Bohr Institute, Copenhagen, www.nbi.dk/ChaosBook/, 2003).
70. T.-Y. Li and J. A. Yorke, Period three implies chaos, *Am. Math. Monthly* **82**:985 (1975).
71. N. Metropolis, M. L. Stein, and P. R. Stein, On finite limit sets for transformations of the unit interval, *J. Comb. Theo*. **15**:25 (1973).
72. A. N. Sarkovskii, Co-existence of cycles of a continuous mapping of a line onto itself, *Ukr. Math. Z.* **16**:61 (1964).
73. R. Badii, E. Brun, M. Finardi, L. Flepp, R. Holzner, J. Parisi, C. Reyl, and J. Simonet, Progress in the analysis of experimental chaos through periodic orbits, *Rev. Mod. Phys*. **66**:1389 (1994).